arXiv:1612.00528v1 [astro-ph.GA] 2 Dec 2016

Quasar Host Galaxies and the M_{SMBH} - σ_* Relation

Andrew I. Sheinis[1,2]
and

Ángel R. López-Sánchez[1,3]

ABSTRACT

We analyze the emission line profiles detected in deep optical spectra of quasars to derive the mass of their super-massive black holes (SMBH) following the single-epoch virial method. Our sample consists in 6 radio-loud quasars and 4 radio-quiet quasars. We carefully fit a broad and narrow Gaussian component for each bright emission line in both the Hβ (10 objects) and Hα regions (5 objects). We find a very good agreement of the derived SMBH masses, $M_{\rm SMBH}$, using the fitted broad Hβ and Hα emission lines. We compare our $M_{\rm SMBH}$ results with those found by previous studies using the reverberation mapping technique, the virial method and X-ray data, as well as those derived using the continuum luminosity at 5100 Å. We also study the relationship between the $M_{\rm SMBH}$ of the quasar and the stellar velocity dispersion, σ_*, of the host galaxy. We use the measured $M_{\rm SMBH}$ and σ_* to investigate the $M_{\rm SMBH}$ – σ_* relation for both the radio-loud and radio-quiet subsamples. Besides the scatter, we find a good agreement between radio-quiet quasars and AGN+quiescent galaxies and between radio-loud quasars and AGN. The intercept in the latter case is 0.5 dex lower than in the first case. Our analysis does not support the hypothesis of using σ([O III] λ5007) as a surrogate for stellar velocity dispersions in high-mass, high-luminosity quasars. We also investigate the relationship between the 5 GHz radio-continuum luminosity, $L_{5\,\rm GHz}$, of the quasar host galaxy with both $M_{\rm SMBH}$ and σ_*. We do not find any correlation between $L_{5\,\rm GHz}$ and $M_{\rm SMBH}$, although we observe a trend that galaxies with larger stellar velocity dispersions have larger 5 GHz radio-continuum luminosities. Using the results of our fitting for the narrow emission lines of [O III] λ5007 and [N II] λ6583 we estimate the gas-phase oxygen abundance of six quasars, being sub-solar in all cases.

Subject headings: Galaxies: Active – Galaxies: Quasars – Galaxies: Kinematics – Galaxies: Super-massive black hole – Galaxies: abundances

1. Introduction

How super-massive black holes (SMBH) grow in the center of galaxies is intimately related to how galaxies are formed and evolve. Over the last decade an increasing number of both theoretical and observational studies have provided a better understanding of the physical connection between SMBH and galaxy evolution, particularly since the discovery that all galaxies with a bulge contain a SMBH (Kormendy & Richstone 1995). However, the fundamental observational evidence is the relationship found between the SMBH mass, $M_{\rm SMBH}$, and the host galaxy stellar velocity dispersion –bulge stellar velocity dispersion–, σ_*, which was first predicted by Silk & Rees (1998) and Fabian (1999) and later verified in both active (Gebhardt et al. 2000a; Ferrarese et al. 2001; Nelson et al. 2004; Onken et al. 2004; Dasyra et al. 2007; Woo et al. 2010, 2013; Graham et al. 2011;

[1]Australian Astronomical Observatory, PO Box 915, North Ryde, NSW 1670, Australia.

[2]Sydney Institute for Astronomy (SIfA), School of Physics, The University of Sydney, NSW 2006, Australia.

[3]Department of Physics and Astronomy, Macquarie University, NSW 2109, Australia.

Park et al. 2012) and quiescent (Ferrarese & Merritt 2000; Gebhardt et al. 2000b; Tremaine et al. 2002; Gültekin et al. 2009; McConnell et al. 2011; McConnell & Ma 2013) galaxies. As the bulge extends by several orders of magnitude outside the gravitational influence of the SMBH, the $M_{\rm SMBH}$- σ_* correlations suggests that both the bulge and SMBH coevolve (Kormendy, Gebhardt & Richstone 2000). Furthermore, the inclusion of active galactic nuclei (AGN) feedback, or an equivalent energetic source to quench star formation above a critical halo mass, in semi-analytic galaxy formation models (Cattaneo et al. 2006; Dekel & Birnboim 2006) matches the galaxy demographics and bimodality of properties observed in large surveys –SDSS: Kauffmann et al. (2003b,a); Hogg et al. (2003); Baldry et al. (2004); Heavens et al. (2004); Cid Fernandes et al. (2005); GOODS: Giavalisco et al. (2004); COMBO-17: Bell et al. (2004); DEEP/DEEP2: Koo et al. (2005); MUNICS: Drory et al. (2001); FIRES: Labbé et al. (2003); K20: Cimatti et al. (2002); GDDS: McCarthy et al. (2004). However, the details of the physical processes that make the connection between the growth mechanisms of the black hole and galaxy, such as how AGN energy interacts with and is dissipated by surrounding halo gas, are not yet known.

We seek to clarify if there is an unique $M_{\rm SMBH}$– σ_* relationship or if it differs for different kind of objects. For example, some analyses suggest a morphological dependence of the $M_{\rm SMBH}$– σ_* relation between low-mass –usually late-type– and high-mass –early-type– quiescent galaxies (e.g. Greene et al. 2010; McConnell & Ma 2013). It has been also found that both barred galaxies and galaxies hosting pseudobulges do not follow the standard $M_{\rm SMBH}$– σ_* relation (e.g. Graham 2008a,b; Graham & Li 2009; Hu et al. 2008; Gadotti & Kauffmann 2009; Kormendy, Bender & Cornell 2011). Furthermore, some morphological deviations have been reported in AGN (e.g. Graham & Li 2009; Graham et al. 2011; Woo et al. 2010, 2013; Mathur et al. 2012; Park et al. 2012). However, it is not clear yet if such deviations in the M_{SMBH}-σ_* relation exist in the high-mass (and high velocity dispersion) end, as claimed by several authors (Dasyra et al. 2007; Watson et al. 2008) but not confirmed by others (Grier et al. 2013). Numerical models, as those presented by King (2010) and Zubovas & King (2012), suggest that the $M_{\rm SMBH}$–σ_* relationship is not unique and it may even depend on the environment.

The stellar velocity dispersion in the host galaxies is estimated using the stellar absorption lines in galaxy spectra of the quiescent galaxies. This in fact was the method first used to discover the M_{SMBH}-σ_* relation (Gebhardt et al. 2000a; Ferrarese & Merritt 2000). For bonafide quasars ($M_V < -23$), the quasar can be up to 3 magnitudes brighter than the integrated light from the host (Miller & Sheinis 2003), which complicates the extraction of the stellar absorption lines from the host. Thus a limited number of studies have been possible for bright quasars (Wolf & Sheinis 2008). Shields et al. (2003) developed one method of estimating the M_{SMBH}-σ_* relation using the results of Nelson & Whittle (1996), who found a correlation between [O III] emission linewidth and σ_*. This method used the velocity dispersion of [O III] as a surrogate for stellar velocity dispersion and has shown that AGN and quasars follow the M_{SMBH}-σ_* relation at a wide range of redshifts, albeit with large scatter. However, there have been some indications that radio-loud quasars may not follow this trend (Laor 2000; McLure & Jarvis 2004).

Black hole masses are derived in a number of different ways (see Czerny & Nikołajuk 2010; Shen 2013, for recent reviews). Gebhardt et al. (2000b) computed them through simulations of galaxy stellar dynamics for quiescent galaxies. Direct M_{SMBH} measurements should consider both spatial and spectral resolution, being only feasible for nearby galaxies. Recently, Shaposhnikov & Titarchuk (2009) introduced a new method to derive $M_{\rm SMBH}$ based solely on X-ray spectral data. This technique is providing very good results in both quiescent (Shaposhnikov & Titarchuk 2009) and active (Gliozzi et al. 2011) systems.

For AGN, reverberation mapping (Blandford & McKee 1982) is the most accurate method for measuring $M_{\rm SMBH}$. Assuming that the broad emission line region (BLR) is powered by photoionization from the central source, this technique uses the fact that the continuum flux (which arises from the accretion disc or very close to it) varies with time, and is later echoed by changes in the flux of the broad emission lines. The radius of the BLR, R_{BLR}, is then obtained by the cross correlation of the light curves, which provides the

delay time between the broad-line variations and the continuum variations. The SMBH mass is then computed assuming that the BLR is virialized and the motion of the emitting clouds is dominated by the gravitational field of the SMBH (e.g. Ho 1999; Wandel, Peterson & Malkan 1999), $M_{\rm SMBH} = (f\, R_{BLR} {V_{BLR}}^2)/G$. f is a dimensionless factor that accounts for the unknown geometry and orientation of the BLR, V_{BLR} is the dispersion velocity of the gas (which is deduced from the width of the Doppler broadened emission lines). Reverberation mapping allows to probe regions of gas that are only $\sim$0.01 pc in extent. However, this technique requires high-quality spectrophotometric monitoring of an AGN over an extended period of time. The uncertainty of the SMBH masses derived using the reverberation mapping method typically is between 0.4 and 0.5 dex (Peterson 2010; Shen 2013). Reverberation mapping has yielded black hole masses for $\sim$50 AGNs thus far (Kaspi et al. 2000; Peterson et al. 2004; Bentz et al. 2009a). Nevertheless, few reverberation mapping measurements have well-defined velocity-resolved delay maps (e.g. Denney et al. 2009a; Bentz et al. 2010; Grier et al. 2013). The main caveat of this technique is the assumption of the accretion disc morphology (Krolik 2001; Shen 2013), which may be lead to different types of galaxies following somewhat different scaling relations between SMBH mass and bulge properties (Graham 2008a; Greene, Ho & Barth 2008; Greene et al. 2010; Gültekin et al. 2009; McConnell & Ma 2013), leading to accuracy within factors of 2-3 (e.g., Woo et al. 2010; Graham et al. 2011; Park et al. 2012; Grier et al. 2013). Some authors (e.g. Pancoast, Brewer & Treu 2014, and references therein) have recently developed new methods to constrain the geometry and dynamics of the BLR by modeling reverberation mapping data directly. This also allows to measure SMBH masses independent of a virial coefficient. In particular, Pancoast, Brewer & Treu (2014) claim they can recover the black hole mass to 0.05 – 0.25 dex uncertainty.

The single-epoch virial method has been calibrated using reverberation mapping (e.g. Kaspi et al. 2000, 2005; Greene & Ho 2005; Bentz et al. 2006; Vestergaard & Peterson 2006; McGill et al. 2008; Bentz et al. 2009b, 2013; Shen & Liu 2012). This technique, which assumes that the BLR gas is virialized and hence follows the virial relation, assumes a radius-luminosity relation of the form $R_{BLR} \propto L^{\alpha}$. The coefficients of this relation are determined from estimates of a sample of AGNs for which reverberation mapping data are available. For the case of the broad Hβ emission line, it has been established $\alpha \sim 0.52 - 0.56$. Individual black hole masses derived using reverberation mapping differ from those derived by the radius-luminosity relation of the BLR by up to 0.5 dex (e.g. McLure & Jarvis 2002; Peterson et al. 2004; Vestergaard & Peterson 2006; Kim et al. 2008).

This study uses the single-epoch virial method to derive the SMBH of a sample of luminous quasars via a careful analysis of the Hβ and Hα emission line profiles. The main objective is to investigate the M_{SMBH}-σ_* relation on these bright quasars. This paper is organized as follows. Section 2 describes our sample, which consists in 6 radio-loud quasars and 4 radio-quiet quasars. Section 3 presents the analysis of the data and how the SMBH masses have been estimated. Our results are discussed in Sect. 4, which compares our mass estimations with those reported in the literature; explores the M_{SMBH}-σ_* and the M_{SMBH}-QSO radio-luminosity relations; as well as discusses the nature of the radio-loud and radio-quiet quasars. In Sect. 4 we also compare the stellar velocity dispersions with the FWHM of broad [O III] emission and, when possible, estimate the gas-phase metallicity of the host galaxies using the narrow emission lines. Finally Sect. 5 provides the conclusions of our analysis.

2. Data selection

Here we analyse the sample of 10 nearby and luminous quasars studied by Wolf & Sheinis (2008). These authors defined their sample following Bahcall et al. (1997) observations of bright ($M_V < -29.9$), low-z ($z \leq 0.20$), and high galactic latitude ($|b| > 35^{\circ}$) quasars, with the addition of a few objects from Dunlop et al. (2003) and Guyon, Sanders & Stockton (2006) with the same characteristics. However, this sample included only 3 radio-loud quasars, and hence 6 extra objects with redshift $0.20 < z < 0.30$ (3 of them being radio-loud), also drawn from Bahcall et al. (1997), were added. The same sam-

Table 1

Redshifts, distances, host galaxy velocity dispersions, and radio luminosities of our QSO sample. The redshift is derived from our fit to the radial velocity of the narrow [O III] λ5007 emission line and have an error or $\pm$0.00008. Distances are derived from the redshift assuming a flat cosmology (H_0=70 km s^{-1} Mpc^{-1}, Ω_M = 0.3, and Ω_Λ = 0.7) and have an error of $\pm$0.3 Mpc. Host galaxy velocity dispersions are given by Wolf & Sheinis (2008). For PG 0052+251, σ_* in Wolf & Sheinis (2008) was an upper limit due to the spectral resolution. Radio luminosities has been extracted from Wold et al. (2010).

Quasar Name	Redshift	Distance [Mpc]	Measured σ_* [km s^{-1}]	Avg. Observed Radius [arcsec]	R_e [arcsec]	Ap-Cor σ_* [km s^{-1}]	log ($L_{5\,\mathrm{GHz}}$) [erg s^{-1}]	Radio Activity
PG 0052+251	0.154480	638.0	250 ± 53	3.63	1.8	279 ± 59	39.4	RQ
PHL 909	0.171807	706.5	150 ± 11	4.5	2.3	167 ± 12	40.0	RQ
PKS 0736+017[a]	0.189136	774.5	311± 83	4.5	3.3	342 ± 91	43.0	RL
3C 273[b]	0.157366	649.4	305 ± 57	4.36	3.7	334 ± 62	44.1	RL
PKS 1302-102	0.277831	1112.5	346 ± 72	3.05	1.4	388 ± 80	43.0	RL
PG 1309+355	0.182345	747.9	236 ± 30	4.05	2.0	264 ± 33	41.3	RQ
PG 1444+407	0.267252	1073.0	279 ± 22	3.70	1.3	316 ± 25	39.2	RQ
PKS 2135-147	0.200396	818.3	278 ± 106	3.81	2.6	307 ± 117	42.9	RL
4C 31.63[c]	0.334626	1320.4	290 ± 23	2.0	6.5	301 ± 24	43.3	RL
"	"	"	325 ± 24	2.5	6.5	340 ± 25	"	"
"	"	"	*average*	...	6.5	320 ± 25	"	"
PKS 2349-014	0.173844	714.5	278 ± 54	4.83	4.8	302 ± 59	42.5	RL

[a]Also known as [HB89] 0736+017. [b] Also known as PG 1226+023. [c] Also known as [HB89] 2201+315.

ple of 10 quasars considered by Wolf & Sheinis (2008) was later analysed by Wold et al. (2010) to study the connection between the stellar ages of the host galaxies and the quasar activity. These ten objects are PG 0052+251, PHL 909, PKS 0736+017, 3C 273, PKS 1302-102, PG 1309+355, PG 1444+407, PKS 2135-147, 4C 31.63, and PKS 2349-014.

Nuclear and off-nuclear spectra of seven of the host galaxies of our sample (all but PHL 909, PKS 0736+017 and PG 1309+355) were obtained with the Low Resolution Imaging Spectrograph (Oke et al. 1994) on the Keck telescope during 1996–1997, as detailed in Sheinis (2002) and Miller & Sheinis (2003). An image showing the approximate off-axis slit and fibre positions with respect to each object is shown in Fig. 1 of Wold et al. (2010).

Observed wavelength ranges covered ∼4500–7000 Å at a spectral resolution of $\Delta\lambda$ ∼11 Å (300 km s^{-1}). The spectroscopic data of PHL 909, PKS 0736+017 and PG 1309+355 were obtained in 2007 using the integral field unit (IFU) Sparsepak (Bershady et al. 2004, 2005) which feeds the Bench Spectrograph of the 3.5-m WIYN Telescope[1]. The configuration used provided an observed wavelength coverage of ∼4270–7130 Å at a resolution of $\Delta\lambda$ ∼5 Å (110 km s^{-1}). All spectra were corrected for Galactic extinction using the law of Cardelli, Clayton, & Mathis (1989) and the A_V values from Schlegel, Finkbeiner, & Davis (1998) as listed in the NASA/IPAC Extragalactic Database (NED). More details can be found in Wolf & Sheinis (2008).

Four of the chosen objects, PG 0052+251, PHL 909, PG 1309+355, and PG 1444+407, are radio-quiet (RQ) quasars. The other six objects are radio-loud (RL) quasars. Following Wold et al. (2010), a quasar is defined as radio-loud when $L_{5\,\mathrm{GHz}} \gtrsim 10^{41.5}$ erg s^{-1}. This relatively small sample of quasars is not representative of the local quasar population, which consists of ∼10% RL quasars. While the data presented here consist of half of the nearby and luminous quasars known (following the Bahcall et al. 1997, final sample of

[1]The WIYN Observatory is owned and operated by the WIYN Consortium, Inc., which consists of the University of Wisconsin, Indiana University, Yale University, and the National Optical Astronomy Observatory (NOAO). NOAO is operated for the National Science Foundation by the Association of Universities for Research in Astronomy (AURA), Inc.

20 objects), and includes all the RL quasars in that sample, it is nonetheless a small sample of of only 10 objects. Thus we present the caveat that the initial conclusions drawn from our analysis and comparison between the properties of RL and RQ quasars are based on the small sample and will be better confirmed when more objects with the same characteristics are considered in an upcoming paper.

3. Analysis

3.1. Stellar Velocity Dispersions

Stellar velocity dispersions ($\sigma_\star$) of the host galaxies were presented in Wolf & Sheinis (2008). $\sigma_\star$ were derived from stellar absorption lines in the host galaxies by fitting a stellar template (main sequence A stars through K giants) that has been convolved with a gaussian profile to the off-nuclear, scatter-subtracted galaxy spectrum in pixel space using the code of Karl Gebhardt (Gebhardt et al. 2000a, 2003). The wavelength range of 3850–4200 Å, which contains the Ca II H,K (3968, 3934 Å) absorption lines, was used for the velocity dispersion fits.

Velocity dispersion uncertainties were calculated through Monte Carlo simulations by adding Gaussian noise to each pixel in the final template, which has a very high S/N, at a level such that the mean matches the noise in the initial galaxy spectrum and the standard deviation is given by the rms of the initial fit. The velocity dispersion was then measured for 100 noise realizations and the mean and standard deviation of these results provide the measured velocity dispersion and its 1σ uncertainty.

Because velocity dispersion varies with galaxy radius, to match the comparison data all host galaxy velocity dispersions were corrected from the radius at which $\sigma_\star$ was measured to a radius of $R_e/8$ using the correction in Bernardi et al. (2003) and Jorgensen, Franx & Kjaergaard (1995),

$$\sigma_{\star,corr} = \sigma_{\star,meas}\left(\frac{R_{obs}}{R_e/8}\right)^{0.04}. \quad (1)$$

Aperture-corrected values for the host galaxies and average observed radii are compiled in Table 1. For 4C 31.63 two $\sigma_\star$ values were obtained at different radii. For our analysis we will use the average value, as indicated in the table.

Eight of our objects are found in elliptical galaxies and two (PG 0052+251, PG 1309+355) in spirals (see Table 1 in Wolf & Sheinis 2008). The determination of $\sigma_\star$ did not consider galaxy rotation, which may induce to overestimate its real value up to $\sim$15 – 20% (this actually depends on the inclination angle of the rotating disk and the maximum rotation velocities) in spiral galaxies (Kang et al. 2013; Woo et al. 2013). The effect of rotation is particularly important when using the integrated flux of galaxy, however the the detailed procedure carried out by Wolf & Sheinis (2008) to derive $\sigma_\star$ used off-nuclear regions, so we consider the effect of galaxy rotation to be small.

3.2. Black hole masses

As explained in the introduction, the mass of a super massive black hole, $M_{\rm SMBH}$ can be determined via the kinematics of the ionized gas surrounding it. The virial method assumes that if the full width half-maximum (FWHM) of the broad emission lines reflects a Keplerian motion of the gas in the BLR, $M_{\rm SMBH}$ can be estimated from

$$M_{\rm SMBH} = f \times \frac{R_{\rm BLR} V_{\rm BLR}^2}{G}, \quad (2)$$

where G is the gravitational constant, $R_{\rm BLR}$ is the radius of the BLR, $V_{\rm BLR}$ is the rotational velocity of the ionized gas and f is a dimensionless factor that accounts for the unknown geometry and orientation of the BLR. $V_{\rm BLR}$ is estimated from the FWHM of the Hα or Hβ emission lines, while $R_{\rm BLR}$ is determined using the monochromatic continuum luminosity of the host galaxy at 5100 Å, L_{5100} (Kaspi et al. 2000, 2005). As the continuum luminosity is correlated with the luminosities of the Hα and Hβ emission lines, the mass of the SMBH can be estimated using both the luminosities and the FWHM of the broad H I Balmer line. Although more recent calibrations are available (i.e. McGill et al. 2008; Assef et al. 2011; Park et al. 2012) we prefer to use Greene & Ho (2005) as they provide consistent equations for Hα, Hβ, and L_{5100}. These equations are:

$$M_{\rm SMBH} = (3.6 \pm 0.2) \times 10^6 \times \left(\frac{L_{\rm H\beta}}{10^{42}\,{\rm erg\,s^{-1}}}\right)^{(0.56\pm0.02)} \times \left(\frac{\rm FWHM_{H\beta}}{10^3\,{\rm km\,s^{-1}}}\right)^2 [M_\odot], \quad (3)$$

and

$$M_{\rm SMBH} = 2.0^{+0.4}_{-0.3} \times 10^6 \times \Big(\frac{L_{\rm H\alpha}}{10^{42}\,{\rm erg\,s^{-1}}}\Big)^{(0.55\pm0.02)} \times \Big(\frac{\rm FWHM_{H\alpha}}{10^3\,{\rm km\,s^{-1}}}\Big)^{(2.06\pm0.06)} \quad [M_\odot]. \quad (4)$$

Greene & Ho (2005) assumed the following virial formula for the SMBH mass:

$$M_{\rm SMBH} = (4.4 \pm 0.2) \times 10^6 \times \Big(\frac{\lambda L_{5100}}{10^{44}\,{\rm erg\,s^{-1}}}\Big)^{(0.64\pm0.02)} \times \Big(\frac{\rm FWHM_{H\beta}}{10^3\,{\rm km\,s^{-1}}}\Big)^{2} \quad [M_\odot], \quad (5)$$

which uses the continuum luminosity at rest frame wavelength 5100 Å, λL_{5100}, and the FWHM of the broad Hβ emission line, $\rm FWHM_{H\beta}$.

Here, we use the optical spectra of our sample of quasars to analyse the emission line profiles of the Hβ and [O III] $\lambda\lambda$4959,5007 emission lines, plus the Hα and [N II] $\lambda\lambda$6548,6583 emission lines if also observed, to derive their SMBH masses. We fitted a narrow and a broad Gaussian components –expressed as $G = p \times \exp[-0.5 \times (\frac{\lambda - c}{\sigma})^2]$, being p the peak of the Gaussian, σ its width and c its central wavelength– in each of these emission lines over a continuum. When detected, we also considered other broad and narrow emission lines such as [O I] λ6300, [He I] λ6678, or [S II] $\lambda\lambda$6717,6731. In particular, for many cases it was important to include a broad and narrow emission line component around λ4686, which may be attributed to the high-ionization He II λ4686 emission line and which may cause an overestimation of the continuum and the Hβ real flux and therefore complicates the proper measurement of the Hβ line dispersion (e.g. Decarli et al. 2008; Denney et al. 2009b). The inclusion of a broad component for the NLR lines is justified by the finding of outflows of ionized gas around AGNs and, in particular, around RL quasars (e.g. Nesvadba et al. 2006; Holt, Tadhunter & Morganti 2008; Fu & Stockton 2009; Husemann et al. 2014), with radial velocities of the ionized gas exceeding more than 500 $\rm km\,s^{-1}$. These outflows of ionized gas have been interpreted as evidence of AGN feedback (Liu et al. 2013a,b; Husemann et al. 2014; Zakamska & Greene 2014). The presence of broad components in the emission lines observed in galaxy spectra is now commonly taken into account by on-going 3D spectroscopic surveys, for example, the LZIFU code that the "Sydney-AAO Multi-IFU Galaxy Survey" (SAMI, Croom et al. 2012; Bryant et al. 2015) has developed (Ho et al. 2014), or in the kinematical analysis of the ionized gas in the galaxies of the "Calar-Alto Legacy Integral Field Area" (CALIFA, Sánchez et al. 2012; García-Benito et al. 2015) Survey (García-Lorenzo et al. 2015). Furthermore, a broad Fe II emission should be considered between Hβ and [O III] λ4959 (e.g. Boroson & Green 1992; Park et al. 2012). The broad Fe II is a sum of several blended Fe II lines that span from 3535 to 7530 Å. We use the template Fe II emission spectrum of the narrow emission-line type Seyfert 1 galaxy I Zw 1 provided by Véron-Cetty, Joly & Véron (2004), which was convoluted to the spectral resolution of each particular quasar spectrum, to remove the contribution of the Fe II lines in the range 4700-5100 Å. We note that not all the emission attributed to Fe II lines in the quasar spectra was always removed, and that the broad [O III] lines are sometimes likely fitting these residuals.

The procedure we followed for performing the fitting in the Hβ region was the following:

1. First, we fit the continuum and broad and narrow components around the He II λ4686 emission line (if any).

2. Then, we use the template provided by Véron-Cetty, Joly & Véron (2004) to scale the Fe II template spectrum only considering the lines in the range 4500-5100 Å by minimizing the fit residuals. However, as I Zw 1 is a narrow line emission galaxy type Seyfert 1, we use the broad Fe II lines observed in the 4500-4700 Å range for providing a broadening to the Fe II template spectrum. In any case the contribution of the Fe II lines in the broad Hβ range is small, typically between 1–6% of the total flux of the derived broad Hβ flux (see Table 2).

3. Then we fit the spectral profile between Hβ and [O III] using three broad components: the broad Hβ and the broad [O III] lines. All these components must have sigma > 10 Å to assure that we are not fitting any narrow line. The scale factor for the Fe II template

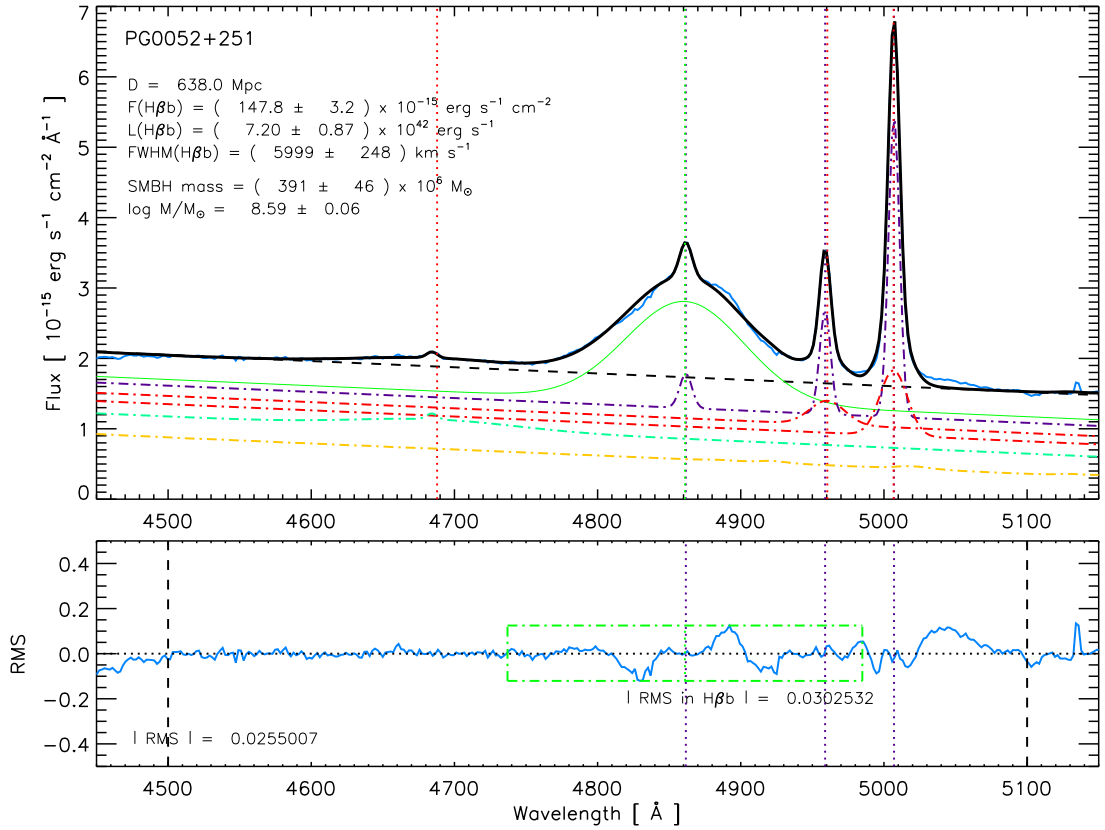
PG0052+251
D = 638.0 Mpc
F(Hβb) = (147.8 ± 3.2) x 10^-15 erg s^-1 cm^-2
L(Hβb) = (7.20 ± 0.87) x 10^42 erg s^-1
FWHM(Hβb) = (5999 ± 248) km s^-1
SMBH mass = (391 ± 46) x 10^6 M⊙
log M/M⊙ = 8.59 ± 0.06
Flux [10^-15 erg s^-1 cm^-2 Å^-1]
RMS
| RMS in Hβb | = 0.0302532
| RMS | = 0.0255007
Wavelength [Å]

Fig. 1.— (*Top panel*) Fit to the emission line profiles of PG 0052+251 observed around the Hβ region. The blue line is the observed spectrum of the quasar, while the black line is the best fit to the data. The black dashed line is the fit to the continuum. Dotted magenta lines indicate the center of the narrow-components for Hβ and [O III] $\lambda\lambda$4959, 5007. Dotted red lines indicate the center of all the broad components but Hβ. The center of the broad Hβ line is plotted by a green dotted line. The continuous green line shows the broad Hβ gaussian. The dotted-dashed magenta line represents the narrow-component spectrum. The dotted-dashed red lines correspond to the broad [O III] lines. The dotted-dashed green line represents the broad and narrow He II λ4686 lines. The dotted-dashed yellow line shows the template Fe II spectrum (Véron-Cetty, Joly & Véron 2004) scaled for this object considering the 4500-5100 Å range. Some derived properties of the fit are shown in the top left corner. (*Bottom panel*) The blue line represents the *rms* of our fit. The fit has been done within the region between the vertical dashed lines. The average value of the *rms* is shown in the bottom left corner. The green dashed box indicates the region used to estimate the *rms* of the broad Hβ component; its average value is also shown. Dotted magenta lines indicate the center of the narrow-components for Hβ and [O III] $\lambda\lambda$4959, 5007.

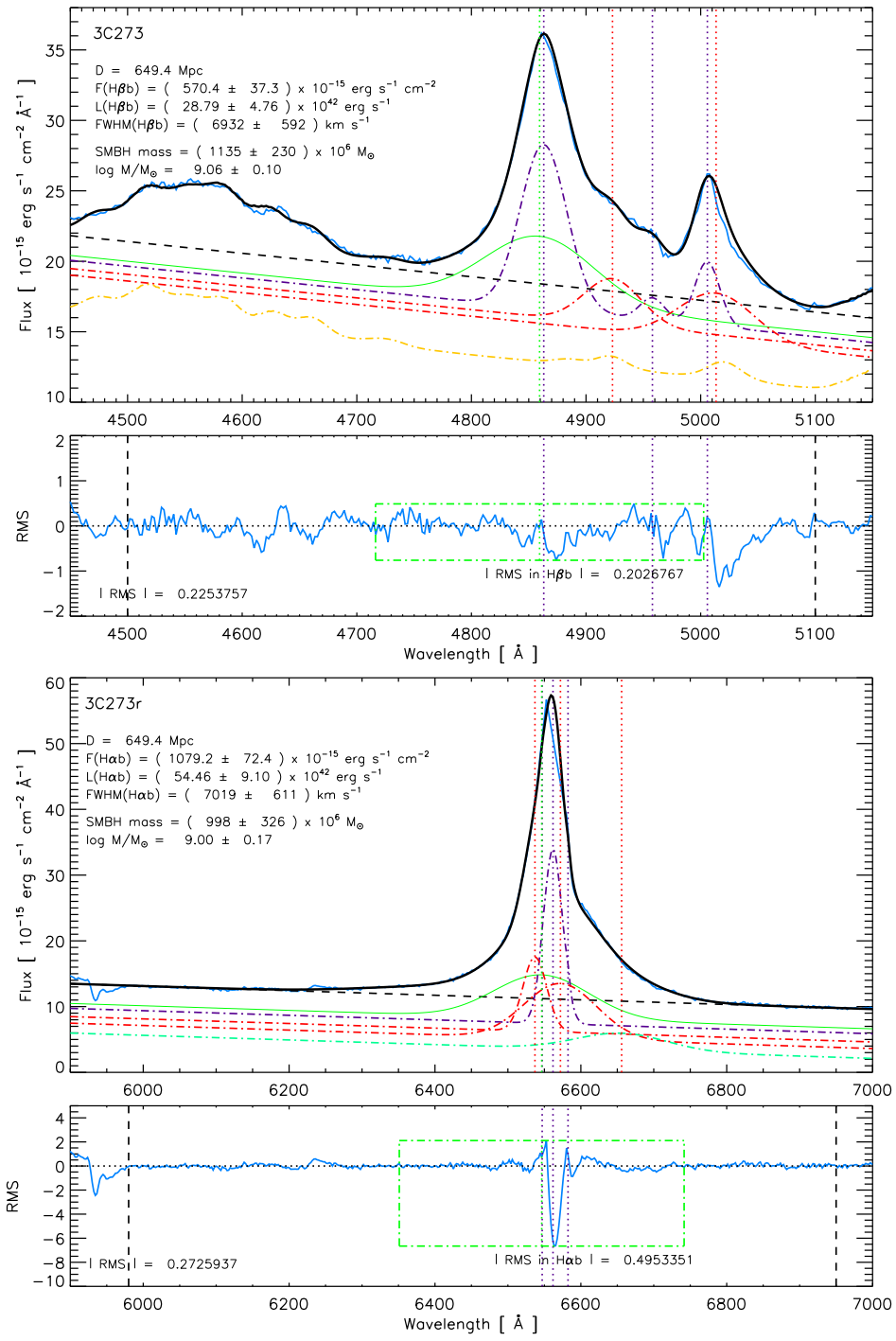
3C273
D = 649.4 Mpc
F(Hβb) = (570.4 ± 37.3) x 10^-15 erg s^-1 cm^-2
L(Hβb) = (28.79 ± 4.76) x 10^42 erg s^-1
FWHM(Hβb) = (6932 ± 592) km s^-1
SMBH mass = (1135 ± 230) x 10^6 M⊙
log M/M⊙ = 9.06 ± 0.10
Flux [10^-15 erg s^-1 cm^-2 Å^-1]
RMS
| RMS | = 0.2253757
| RMS in Hβb | = 0.2026767
Wavelength [Å]
3C273r
D = 649.4 Mpc
F(Hαb) = (1079.2 ± 72.4) x 10^-15 erg s^-1 cm^-2
L(Hαb) = (54.46 ± 9.10) x 10^42 erg s^-1
FWHM(Hαb) = (7019 ± 611) km s^-1
SMBH mass = (998 ± 326) x 10^6 M⊙
log M/M⊙ = 9.00 ± 0.17
Flux [10^-15 erg s^-1 cm^-2 Å^-1]
RMS
| RMS | = 0.2725937
| RMS in Hαb | = 0.4953351
Wavelength [Å]

Fig. 2.— Fit to the emission line profiles of 3C 273 around the Hβ region (top) and the Hα region (bottom). The lines are the same described in Fig. 1, following a similar description for the Hα fit (the blue line is the observed spectrum, the black line is our best fit, dotted red lines are the center of the broad components but Hα, which is plotted by a green dotted line; the continuous green line is the broad Hα Gaussian, the dotted-dashed magenta line is the narrow Hα line; the dotted-dashed red lines are the broad [N II] lines; and the dotted-dashed green line is a broad He I λ6678 line).

TABLE 2

DETAILS OF THE FLUX CONTRIBUTIONS OF THE He II, Fe II AND BROAD Hβ LINES TO THE FITS IN THE 4500-5100 Å REGION.

Object	Fe II	He II lines		% Fe II		% He II		% Hβ broad	
		Broad	Narrow	All	broad Hβ	All	broad Hβ	All	broad Hβ
PG 0052+251	VERY FAINT[a]	VERY FAINT	YES	1.2	0.9	6.9	1.8	56.4	81.0
PHL 909	FAINT	VERY FAINT	YES	7.9	2.6	4.3	0.7	51.4	64.2
PKS 0736+017	YES	YES	YES	17.0	5.7	15.0	2.7	40.5	77.3
3C 273	YES	NO	NO	34.5	5.6	0.0	0.0	20.4	34.1
PKS 1302-102	YES	NO	NO	37.4	4.3	0.0	0.0	38.7	82.2
PG 1309+355	YES	NO	YES	29.2	2.8	0.4	0.0	42.6	69.9
PG 1444+407	YES	NO	NO	54.1	7.7	0.0	0.0	27.9	66.1
PKS 2135-147	VERY FAINT[a]	VERY FAINT	YES	4.0	0.8	4.2	1.7	43.6	46.3
4C 31.63	YES	NO	NO	38.0	5.8	0.0	0.0	43.9	84.5
PKS 2349-014	FAINT	NO	VERY FAINT	8.2	1.7	0.3	0.0	46.8	75.2

[a]A fit without considering the Fe II template essentially provides the same result.

spectrum is also included in the minimization of the fit residuals.

4. After that, we add the three narrow emission lines corresponding to the nebular Hβ and [O III] emission. We forced sigma to be the same in the three lines. As the integrated flux of the [O III] emission lines is fixed by theory (Osterbrock & Ferland 2006), we also forced that F[O III] λ4959 = 0.3467×F[O III] λ5007. We then search for those three narrow Gaussians that minimized the residuals.

5. If the narrow Hβ emission seems to be broader than the [O III] lines, we then fit only this line to get a better solution.

6. We now search for the best combination of narrow+broad Gaussians that fits the [O III] lines, again forcing the same sigma in both narrow lines and F[O III] λ4959 = 0.3467×F[O III] λ5007 in the narrow lines.

7. Finally, we slightly change the parameters of all Gaussians and search for the combination that minimizes the residuals but keeping all assumptions considered before (e.g., same sigma for narrow lines). This would be our best fit.

We note that, although it is not usually considered (e.g. Mezcua et al. 2011; Fogarty et al. 2012; Ho et al. 2014; Wild et al. 2014; Sánchez et al. 2015), the flux of the broad [O III] lines could be also fixed following the theory (Osterbrock & Ferland 2006). However we have considered this assumption for the most challenging case, 3C 273 and note that this assumption leads to a slightly worse fit and it does not materially change the results for the derived values (FWHM, flux, and SMBH mass).

The results of the Gaussians which are providing the best fits are listed in Table 3, while the plots showing these fits and their *rms* are compiled in Figures 1, 2, and 10 to 15. We note that some of the residuals obtained follow from some small asymmetry of the broad Hβ line or the broad [O III] λ5007 line (broad asymmetric wings). These asymmetric features can be fitted using Gauss-Hermite polynomials (e.g, see Park et al. 2012), however their contribution is rather small (few %), so we just include this discrepancy in our final error budget.

We follow a similar procedure for fitting the Hα region. In this case, we force F[N II] λ6548 = 0.3402×F[N II] λ6583 for the narrow emission line components. The spectra resolution of some of the spectra obtained around the Hα region is low enough to reduce the accuracy of the fitting (particularly in 4C 31.63), but this uncertainty is included in the error budget of the broad Hα line. In any case, as we will discuss below, the Hα-based SMBH masses agree very well with the Hβ-based SMBH masses in all objects (differences smaller than 0.06 dex).

Finally, we applied Eqs. 3 and 4 to derive the

Table 3

Results of the best fits to the emission line profiles of our quasar spectra. For each emission line we provide the results for both the narrow (n) and the broad (b) components. We provide the σ, central wavelength, c, and peak, p, of a Gaussian fit, $G = p \times \exp\left[-0.5 \times (\frac{\lambda - c}{\sigma})^2\right]$. We express p in units of 10^{-16} erg s^{-1} cm^{-2}, σ and c in units of Å. For some few objects we added an extra broad component (e) in Hβ or Hα, which provides a most robust fit to the data.

Quasar	Comp.	He II λ4686			Hβ			[O III] λ4959			[O III] λ5007		
		σ	c	p	σ	c	p	σ	c	p	σ	c	p
PG0052+251	n	3.69	4684.1	0.836	4.30	4861.4	4.86	3.83	4958.7	14.8	3.83	5006.8	42.8
	b	56.1	4687.7	1.22	41.3	4860.8	14.3	12.2	4960.3	3.37	9.54	5006.5	9.25
PHL909	n	5.78	4687.9	0.482	4.90	4861.0	0.842	4.90	4958.1	3.32	4.90	5006.7	9.58
	b	···	···	···	47.0	4862.6	6.10	21.8	4944.1	2.52	28.1	4989.6	2.86
PKS0736+017	n	5.48	4687.7	0.276	9.15	4863.3	1.05	4.90	4958.9	0.779	4.90	5006.8	2.49
	b	···	···	···	21.8	4866.9	3.81	23.5	4939.2	0.625	36.4	5029.4	0.442
3C273	n	···	···	···	20.2	4864.0	116.6	10.8	4958.9	15.7	10.8	5006.8	45.4
	b	···	···	···	47.7	4860.4	47.7	24.7	4924.0	32.3	33.3	5014.4	34.2
PKS1302-102	n	···	···	···	5.71	4861.6	1.74	5.03	4958.0	2.18	5.03	5006.1	5.41
	b	···	···	···	29.3	4867.9	5.59	13.3	4940.6	1.19	14.6	5003.7	2.52
PG1309+355	n	10.5	4686.7	3.48	4.01	4861.6	18.9	4.01	4958.7	23.1	4.01	5006.7	66.6
	b	···	···	···	43.9	4870.7	40.0	14.6	4954.3	15.5	12.3	5002.4	39.8
PG1444+407	n	···	···	···	12.4	4863.3	8.53	5.14	4958.9	0.771	5.14	5004.0	3.70
	b	···	···	···	29.4	4867.5	12.1	15.9	4941.2	2.56	28.5	5016.6	2.07
PKS2135-147	n	5.04	4686.0	2.26	4.31	4861.8	7.53	4.03	4959.1	31.1	4.03	5006.8	89.7
	b	125.7	4691.4	0.810	58.2	4867.6	10.0	13.6	4961.0	2.33	12.8	5011.1	7.36
4C31.63	n	···	···	···	6.03	4870.7	1.73	5.28	4960.1	2.52	5.28	5006.2	7.85
	b	···	···	···	26.2	4879.0	21.3	13.4	4946.8	4.13	39.3	5018.0	2.82
PKS2349-014	n	4.79	4686.8	0.168	6.09	4863.1	2.01	4.40	4959.0	4.55	4.40	5006.8	13.1
	b	···	···	···	41.66	4862.6	5.13	16.1	4956.1	0.990	16.9	5004.7	2.52

Object	Comp.	[N II] λ6548			Hα			[N II] λ6583			He I λ6678		
		σ	c	p	σ	c	p	σ	c	p	σ	c	p
3C273	n	2.73	6548.0	5.02	13.0	6562.8	265.1	2.73	6583.4	14.8	···	···	···
	b	16.2	6538.0	113.0	65.1	6547.3	66.1	49.6	6573.0	83.9	62.1	6656.9	26.2
PKS1302-102	n	5.69	6547.2	0.841	5.69	6563.9	6.55	5.69	6584.2	2.43	···	···	···
	b	6.37	6548.6	3.63	39.9	6568.9	11.2	9.38	6577.2	1.71	14.8	6679.1	1.77
PKS2135-147	n	5.72	6547.3	2.70	5.72	6562.1	25.4	5.72	6582.7	7.78	···	···	···
	b	37.6	6467.0	9.50	73.2	6575.7	24.7	46.3	6578.8	10.6	9.51[a]	6723.3[a]	2.93[a]
4C31.63	n	17.42	6525.5	1.01	17.4	6560.6	3.32	17.4	6574.9	2.97	···	···	···
	b	13.22	6546.4	10.6	39.8	6567.5	27.5	19.3	6570.6	15.2	···	···	···
PKS2349-014	n	6.96	6548.1	3.20	6.96	6562.9	11.2	6.96	6582.5	9.39	4.08[b]	6300.6[b]	0.881[b]
	b	16.6	6537.7	8.85	68.0	6583.6	5.03	25.4	6591.3	7.45	11.8[a]	6723.0[a]	1.50[a]

[a]The data correspond to a fit to a broad [S II] λ6717+λ6731 emission line.

[b]The data correspond to a fit to a narrow [O I] λ6300 emission line.

TABLE 4

RESULTS OF THE ANALYSIS OF THE EMISSION LINE PROFILES OF OUR TARGET QUASARS. THE SECOND COLUMN PROVIDES THE BEST *rms* OBTAINED IN THE FIT. THE THIRD COLUMN INDICATES IF THE FIT HAS BEEN PERFORMED TO THE Hβ OR Hα REGION. THE FOURTH AND FIFTH COLUMNS COMPILE THE LUMINOSITY AND FWHM OF THE BROAD Hβ OR Hα EMISSION LINE. COLUMNS SIXTH AND SEVENTH GIVE THE MASS OF THE SMBH DERIVED USING OUR DATA FOLLOWING EQS. 3 AND 4. LAST COLUMN PROVIDES THE STELLAR VELOCITY DISPERSION, $\sigma_\star$, FOR THE ANALYZED GALAXIES, WHICH WAS OBTAINED BY WOLF & SHEINIS (2008).

		Broad Emission Line					
Quasar	*rms*	Line	*L*	FWHM	$M_{\rm SMBH}$	$\log(M_{\rm SMBH}/M_\odot)$	$\log(\sigma_\star)$
	[erg s^{-1} cm^{-2} Å^{-1}]		[10^{42} erg s^{-1}]	[km s^{-1}]	[10^6 $M_\odot$]		[km s^{-1}]
PG0052+251	0.025501	Hβ	7.20 ± 0.87	5999 ± 248	391 ± 46	8.59 ± 0.06	2.45 ± 0.08
PHL909	0.017113	Hβ	4.30 ± 0.58	6830 ± 371	380 ± 52	8.58 ± 0.06	2.22 ± 0.03
PKS0736+017	0.008748	Hβ	1.49 ± 0.20	3157 ± 160	44 ± 5	7.65 ± 0.06	2.53 ± 0.10
3C273	0.225376	Hβ	28.8 ± 4.8	6932 ± 592	1135 ± 230	9.06 ± 0.10	2.52 ± 0.07
	0.272594	Hα	54.5 ± 9.1	7019 ± 611	998 ± 326	9.00 ± 0.17	”
PKS1302-102	0.020744	Hβ	6.07 ± 0.82	4242 ± 234	177 ± 25	8.25 ± 0.07	2.59 ± 0.08
	0.048395	Hα	16.6 ± 2.1	4293 ± 202	188 ± 47	8.28 ± 0.13	”
PG1309+355	0.127747	Hβ	29.51 ± 4.26	6370 ± 410	972 ± 163	8.99 ± 0.08	2.42 ± 0.05
PG1444+407	0.034493	Hβ	12.3 ± 1.8	4261 ± 270	265 ± 42	8.42 ± 0.08	2.50 ± 0.03
PKS2135-147	0.036036	Hβ	11.7 ± 1.8	8440 ± 624	1018 ± 181	9.01 ± 0.08	2.49 ± 0.14
	0.068690	Hα	36.4 ± 4.3	7862 ± 309	1010 ± 274	9.00 ± 0.14	”
4C31.63	0.040863	Hβ	29.24 ± 3.57	3795 ± 160	343 ± 45	8.54 ± 0.06	2.51 ± 0.05
	0.039150	Hα	57.2 ± 6.5	4275 ± 145	369 ± 103	8.57 ± 0.14	”
PKS2349-014	0.013422	Hβ	3.27 ± 0.43	6048 ± 306	255 ± 33	8.41 ± 0.06	2.48 ± 0.08
	0.026210	Hα	5.24 ± 0.90	7295 ± 666	298 ± 81	8.47 ± 0.14	”

SMBH masses using the results provided for the best fit to the broad Hβ and Hα lines, respectively. The luminosities of the broad Hβ and Hα lines were derived just applying the $L = 4\pi D^2 F$ relation. The distance to the quasar, D, was determined from the radial velocity of the narrow [O III] λ5007 emission line, which was also provided by our fit. Both the redshift $z = v_{rad}/c$ and the distance to our objects (estimated assuming a flat cosmology with H_0=70 km s^{-1} Mpc^{-1}, $\Omega_M = 0.3$, and $\Omega_\Lambda = 0.7$) are compiled in Table 1. The FWHM was computed using the standard definition for a Gaussian, FWHM = 2.355×σ. The results for the luminosity and FWHM of the broad Hβ and/or Hα lines of each object are listed in Table 4, which includes the *rms* obtained in our best fit for each case.

Uncertainties were estimated from the *rms* of the fit, which provides an error to the derived values for the flux and the σ of the Gaussians. For estimating the uncertainty in luminosity we also assumed a 5% error in the absolute flux calibration of our spectra. We propagate these errors through the equations to derive the uncertainties of the SMBH masses, taking into account the uncertainties included in Eqs. 3 and 4. The Hα-based SMBH masses have much higher uncertainties than the Hβ-based SMBH masses. In any case, we should keep in mind some caveats, uncertainties, and biases of SMBH masses derived using the virial method (see Sect. 3 in Shen 2013, for a review). For example, as described in the introduction, the actual value of the parameter f introduced in Eq. 2 may vary within a factor of 2–3 depending on the geometry of the BLR. Some other uncertainties are introduced by assuming an unique line profile to infer the underlying BLR velocity structure or considering a single BLR size. The actual effects of the host starlight and the dust reddening (particularly in the blue and UV regimes) are also unknown in many cases, as well as the orientation, isotropy, radiation pressure, and velocity structure of the BLR. Finally, SMBH masses estimated using the virial method may be also affected by the AGN variability.

For completeness, we also estimated the SMBH masses using the continuum luminosity at rest frame wavelength 5100 Å, λL_{5100}, and the FWHM of the broad Hβ emission line derived in our fit, via the virial formula provided by Greene & Ho

TABLE 5

SUPER-MASSIVE BLACK HOLE MASS ESTIMATIONS, IN THE FORM OF $\log(M_{\rm SMBH}/M_\odot)$, FOR THE QUASARS STUDIED IN THIS WORK (TW) AND THEIR ESTIMATIONS FOUND IN THE LITERATURE USING DIFFERENT TECHNIQUES. FORTH COLUMN COMPILES THE AVERAGE VALUE OF THE SMBH MASS DERIVED HERE USING THE FITS TO BOTH Hβ AND Hα BROAD EMISSION LINES. TABLE INCLUDES THE DERIVED f_{5100} FLUXES (SECOND COLUMN AND IN UNITS OF 10^{-15} ERG S^{-1} CM^{-2} Å^{-1}) AND THE SMBH MASS ESTIMATIONS USING THIS VALUE AND FWHM$_{\rm H\beta}$ (THIRD COLUMN).

		TW		Reverberation Mapping Techniques					
Quasar	f_{5100}	L_{5100}	Fits	P04	K08	B09	S03	K08	G11
PG 0052+251	1.50 ± 0.03	8.59 ± 0.06	8.59 ± 0.06	8.56 ± 0.08	8.31 ± 0.10	8.57 ± 0.08	···	···	8.48 ± 0.26
PHL 909	1.224 ± 0.014	8.68 ± 0.06	8.58 ± 0.06	···	···	···	···	9.12 ± 0.20	···
PKS 0736+017	0.430 ± 0.006	7.77 ± 0.06	7.65 ± 0.06	···	···	···	···	8.08 ± 0.20	···
3C 273	11.1 ± 0.4	9.22 ± 0.09	9.04 ± 0.08	8.95 ± 0.08	8.69 ± 0.08	8.95 ± 0.09	8.88	···	···
PKS1302-102	1.30 ± 0.02	8.52 ± 0.07	8.26 ± 0.06	···	···	···	···	8.58 ± 0.30	···
PG 1309+355	8.37 ± 0.05	9.58 ± 0.08	8.99 ± 0.09	···	···	···	8.16	8.38 ± 0.30	···
PG 1444+407	1.58 ± 0.03	10.11 ± 0.10	8.42 ± 0.08	···	···	···	···	8.21 ± 0.20	···
PKS 2135-147	1.486 ± 0.018	9.03 ± 0.07	9.01 ± 0.07	···	···	···	···	8.96 ± 0.20	···
4C 31.63	1.75 ± 0.02	8.56 ± 0.06	8.55 ± 0.05	···	···	···	···	8.43 ± 0.30	···
PKS 2349-014	0.620 ± 0.014	8.68 ± 0.06	8.43 ± 0.06	···	···	···	···	8.55 ± 0.20	···

References. — (P04) Peterson et al. (2004) using reverberation mapping techniques; (K08) Kim et al. (2008) using the reverberation mapping method; (B09) Bentz et al. (2009b) using reverberation mapping techniques; (S03) Shields et al. (2003); (K08) Kim et al. (2008) using the virial method based on the single epoch spectrum; (G11) Gliozzi et al. (2011) using X-ray data.

(2005), see Eq. 5. Table 5 compiles both the f_{5100} measured in our spectra and the SMBH masses using the derived continuum luminosity. The uncertainty of the f_{5100} flux has been estimated using the *rms* of the continuum over the $\lambda\lambda$5075-5125 range and does not include the error in the absolute flux calibration. Errors listed in the mass estimations following this method include the uncertainties in both L_{5100} and FWHM$_{\rm H\beta}$ measurements as well as the uncertainties shown in Eq. 5 and the error in the absolute flux calibration.

4. Discussion

4.1. Mass comparison

We first compared our derived M_{SMBH} values using the fitting to the Hα and Hβ emission line profiles. Top panel of Fig. 3 plots the difference of the logarithm of the masses found using Hα and Hβ profile fitting (y-axis) versus the mass obtained from the Hβ profile fitting (x-axis) for the five quasars we have Hα data. As this panel clearly shows, the Hα-based SMBH masses agree very well with those values derived from the analysis of the Hβ region. The Hα spectra typically have lower spectral resolution than the Hβ spectra, and hence higher uncertainties, thus in these five cases we use an uncertainty-weighted average of both results to minimize the error of our SMBH mass estimations, which we compile in Table 5. The fact that both the Hα-based and the Hβ-based SMBH mass estimations agree well in all cases reinforces the strength of the technique used here to estimate SMBH masses.

Figure 3 also compares our results for the SMBH masses with those values found in the literature. Table 4 compiles the $M_{\rm SMBH}$ masses of our QSO sample found by other authors following different techniques. We note that we checked for a consistent treatment –i.e., similar virial factor used (within 4 - 8%) for computing SMBG masses– when using literature data. Only two of our quasars have an estimation of their SMBH masses using reverberation mapping techniques: 3C 273 and PG 0052+251 (Kaspi et al. 2000; Peterson et al. 2004; Kim et al. 2008; Bentz et al. 2009b). Following Table 5 and the bottom panel of Fig. 3, we see that our results agree well within the errors for PG 0052+251: we derived $\log(M_{\rm SMBH}/M_\odot) = 8.60\pm0.06$, while Peterson et al. (2004) and Bentz et al. (2009b) estimated SMBH masses of 8.56 ± 0.08 and 8.57 ± 0.08, respectively. Kim et al. (2008) derived a somewhat lower mass for the

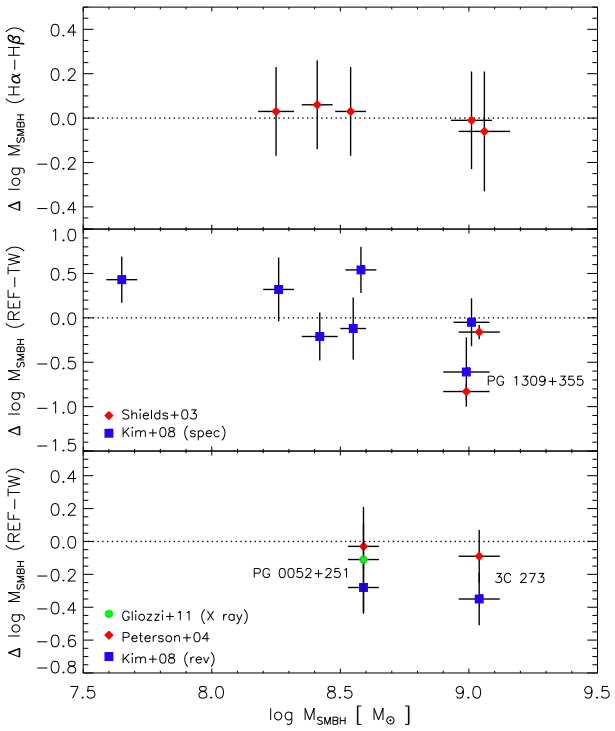

Fig. 3.— (Top) Comparison of the M_{SMBH} derived here using the Hα and Hβ profile fitting. (Middle) Comparison of our M_{SMBH} estimations with the values provided by Shields et al. (2003)–red diamonds– and Kim et al. (2008) –blue boxes–, in both cases derived following the virial method based on the single epoch spectrum. (Bottom) Comparison of our M_{SMBH} estimations with the values provided by Peterson et al. (2004) –red diamonds– and Kim et al. (2008) –blue boxes–, in both cases using reverberation mapping techniques. The value of the M_{SMBH} obtained by Gliozzi et al. (2011) for PG 0052+251 using X ray data is also plotted in this panel –green circle–.

SMBH in this object, 8.31±0.10. Our result for 3C 273 also agrees within the errors with those values reported in the literature using reverberation mapping techniques: we derived $\log(M_{\rm SMBH}/M_{\odot}) = 9.04\pm0.08$ consistently using both the fitting to the Hα and Hβ regions, while Peterson et al. (2004) and Bentz et al. (2009b) estimated 8.95±0.08 and 8.95±0.09, respectively, for this object. However, Kim et al. (2008) provides again a lower mass for the SMBH within 3C 273, $\log(M_{\rm SMBH}/M_{\odot}) = 8.69\pm0.08$. Previous studies of the M_{SMBH} of 3C 273 using the virial method based on a single epoch spectrum also provide lower numbers that we do: Shields et al. (2003) found $\log(M_{\rm SMBH}/M_{\odot}) = 8.88$. We rule out a problem with the absolute flux calibration of our spectrum, as our sample considers other objects that were observed the same night and show no issues with flux calibration. We also consider our analysis, particularly the fitting to the emission line profiles (up to 4 narrow and 5 broad components have been considered), has been performed with more detail than in previous work. However, it is possible that the differing flux measurements of 3C 273 are due to true variations in the emission of this quasar (Lloyd 1984; Hooimeyer et al. 1992; Ghosh et al. 2000; Soldi et al. 2008). Although following the virial hypothesis an increasing (decreasing) of the emission line luminosities will induce a decreasing (increasing) of the rotational velocity of the gas, uncorrelated physical or observational stochastic variations between line width and luminosity (or other effects as described in Sect. 3.2) may also play an important role in determining the SMBH mass of 3C 273.

Middle panel of Fig. 3 compares our SMBH masses with those estimations obtained by Shields et al. (2003) using the M_{SMBH}-σ_* relation based on the [O III] sigma and Kim et al. (2008) using the virial method based on a single epoch spectrum. We see a fairly good correlation for some objects (PKS 1302-102, PKS 2135-147, 4C 31.63, PKS 2349-014) which agree well within the errors but for other objects (PHL 909, PKS 0736+017, PG 1309+355, PG 1444+407) we see poor agreement, well outside the error bars. The worst case is PG 1309+355, SMBH mass estimate disagrees by more than an order of magnitude, between the two methods. We believe our results for this object and for PHL 909 provides the most robust estimate of the MBH mass, as the *rms* of our fits are very low in both cases. Furthermore, as shown in the middle panel of Fig. 3 panel, there appears to be a trend in our fits providing lower SMBH masses than previously estimated in the low-mass end, while obtaining higher SMBH masses than previously estimated in the high-mass end.

The only object in common with the sample analyzed in X rays by Gliozzi et al. (2011) is PG 0052+251 (see bottom panel of Fig. 3). These authors derived $\log(M_{\rm SMBH}/M_{\odot}) = 8.48\pm0.26$,

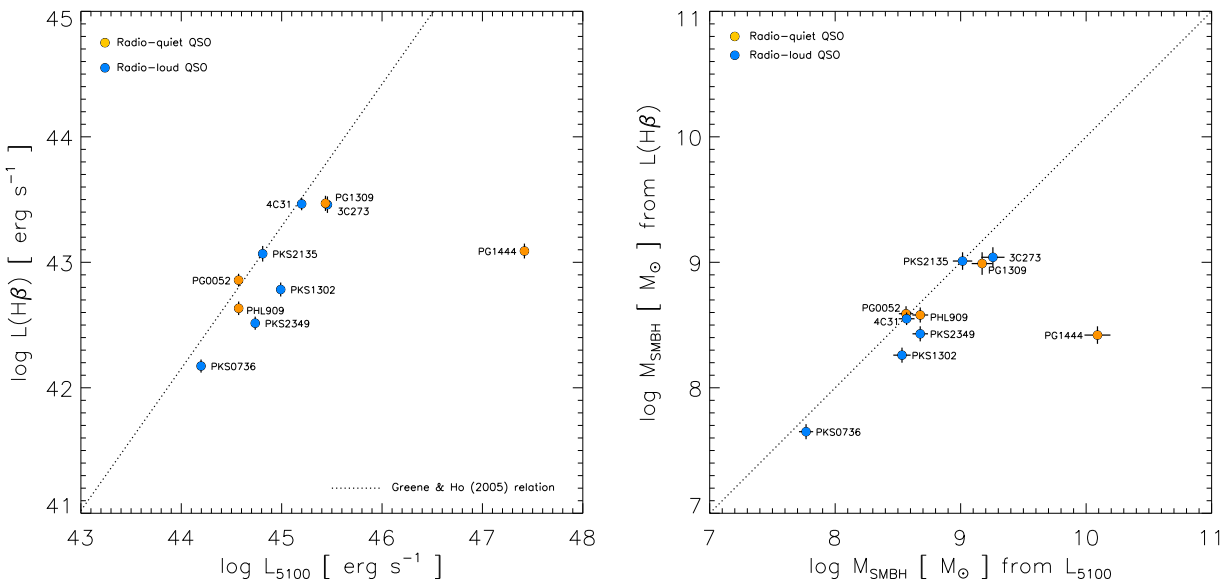

Fig. 4.— (Left) Comparison between the continuum luminosity at rest frame wavelength 5100 Å, λL_{5100}, and the broad Hβ luminosity derived from our fits. The dotted line plots the relationship between both quantities presented by Greene & Ho (2005). (Right) Comparison between the SMBH mass derived using the fits to both the broad Hα and Hβ emission lines and that derived from L_{5100} and FWHM$_{\rm H\beta}$ following Eq. 5. The dotted line indicates $y = x$.

which matches within the errors with our result. This also suggests that the value provided by Kim et al. (2008) using reverberation mapping techniques may be slightly underestimated. If this is also the case for 3C 273, it would explain why our $M_{\rm SMBH}$ estimation is higher than that derived by Peterson et al. (2004); Bentz et al. (2009b) and Kim et al. (2008) using reverberation mapping techniques.

Finally, we also study how well the SMBH masses are recovered when using the continuum luminosity at 5100 Å instead of our fits to the emission line profiles. Left panel of Fig. 4 compares the derived λL_{5100} luminosities with the broad Hβ luminosity obtained in our fits. This panel includes the relationship provided by Greene & Ho (2005). Right panel of Fig. 4 compares the SMBH mass computed using λL_{5100} and that obtained from our fits to the broad emission lines. As we see, all but one of our objects have a relatively good agreement between both SMBH estimations, although masses derived using λL_{5100} seem to be systematically overestimated. Indeed, Greene & Ho (2005) already pointed out this result, emphasizing that the effect is serious for relatively luminous, core-dominated sources and, in particular, radio-loud objects. These authors attributed the enhancement of the optical continuum to jet contamination, although they did not rule out that the enhancement is a consequence of changes in the ionizing spectrum or the covering factor of the ionized gas. Nevertheless there is a large difference in masses –almost 3 orders of magnitude– for PG 1444+407, which is a radio-quiet quasar. We consider that the $M_{\rm SMBH}$ estimation derived using our fit to the Hβ emission line profile is much more robust than that obtained from the continuum luminosity. Indeed, if we assume the SMBH mass derived using the λL_{5100} luminosity as the correct one, PG 1444+407 will lie far away from the rest of the radio-quiet quasars in our subsequent analysis of the $M_{\rm SMBH}$-σ_* relation and $L_{5\,\rm GHz}$-σ_* relation.

4.2. The M_{SMBH}-σ_* relation

Figure 5 plots the M_{SMBH}-σ_* relation found for our sample. Here we distinguish between RL (blue circles) and RQ (yellow circles) galaxies. Figure 5 includes some data points found in the literature: purple stars plot quiescent galaxies data presented by Tremaine et al. (2002), orange

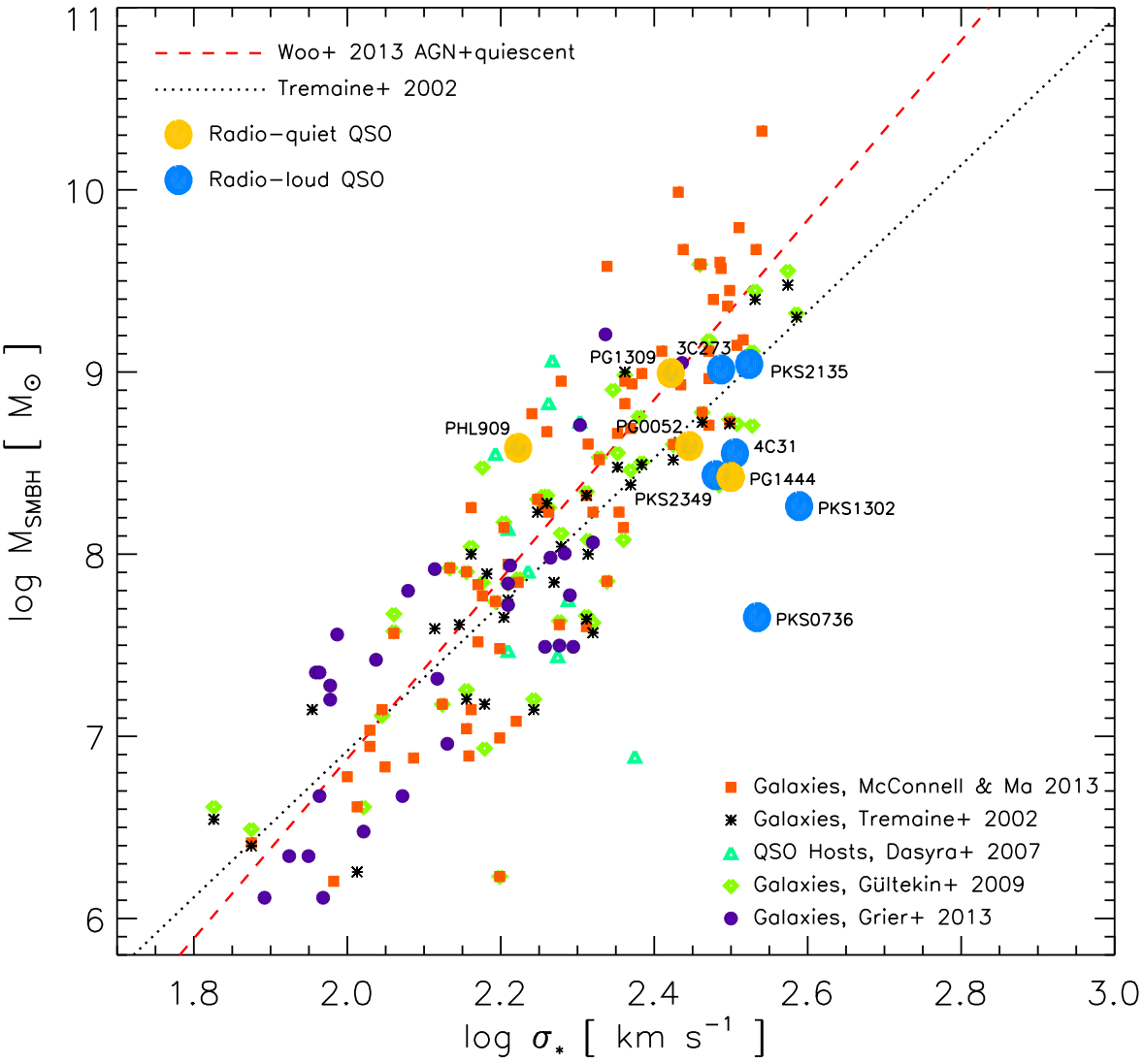

Fig. 5.— M_{SMBH}-σ_* relation. QSO host galaxies from this work are shown as large circles (radio-loud are blue, radio-quiet are yellow). We also plot the data obtained for quiescent galaxies by Tremaine et al. (2002) –black stars– and by McConnell & Ma (2013) –orange squares–, for radio-quiet PG QSO hosts by Dasyra et al. (2007) –cyan triangles–, for galaxies by Gültekin et al. (2009) –green diamonds–, and for galaxies by Grier et al. (2013) –purple circles–. The black dotted line is the relation derived by Tremaine et al. (2002), and the red dashed line is the recent relation provided by Woo et al. (2013) considering both quiescent galaxies and AGN.

squares indicate galaxy data by McConnell & Ma (2013), cyan triangles are the radio-quiet PG QSO hosts data by Dasyra et al. (2007), the green diamonds represent the galaxy data by Gültekin et al. (2009), and purple circles are galaxy data by Grier et al. (2013). The red dashed line is the recent relation provided by Woo et al. (2013), which considers data of both quiescent galaxies and AGN. The standard M_{SMBH}-σ_* relation derived by Tremaine et al. (2002) is also shown with a dotted black line. As we see, the majority of our quasars seem to agree with these relations, although one object (PKS 0736+017) lies somehow below the Tremaine et al. (2002) relation.

It is also interesting to note the large variations in M_{SMBH}-σ_* within the same σ_* interval. For example, both PKS 0736+017 and 3C 273 (two radio-loud quasars) have a very similar velocity dispersion, $\log \sigma_* \sim 2.52$, while their SMBH masses are differing by almost one and a half orders magnitude, $\log M_{SMBH} = 7.65 \pm 0.06$ and 9.04 ± 0.08, respectively.

Some studies (e.g. Grier et al. 2013, and references within) do not find a difference between AGNs and quiescent galaxies on the M_{SMBH}-σ_* relation. However, Woo et al. (2013) investigated the validity of the assumption that quiescent galaxies and active galaxies follow the same relation by updating observational data of both quiescent galaxies and AGN, in the latter case using all available reverberation-mapped AGN. Assuming the standard expression

$$\log\left[\frac{M_{SMBH}}{M_\odot}\right] = \alpha + \beta\left[\frac{\sigma_*}{200\,\mathrm{km\,s^{-1}}}\right], \qquad (6)$$

they derived these relations for the cases of (a) only AGN and (b) AGN + quiescent galaxies. They found that the M_{SMBH}-σ_* of active galaxies (for which $\alpha = 7.31 \pm 0.15$, $\beta = 3.46 \pm 0.61$, and the intrinsic scatter is $\epsilon_0 = 0.41 \pm 0.05$) appears to be shallower than that of AGN+quiescent galaxies (for which $\alpha = 8.36 \pm 0.05$, $\beta = 4.93 \pm 0.28$, and the intrinsic scatter is $\epsilon_0 = 0.43 \pm 0.04$). However, Woo et al. (2013) also state that the two relations are actually consistent with one another, as the two different relations are consistent with the same intrinsic M_{SMBH}-σ_* relation due to selection effects.

Figure 6 compares our QSO datapoints with the Woo et al. (2013) relationships. The left panel considers their M_{SMBH}-σ_* relation for AGN only (purple solid line), whist the right shows their M_{SMBH}-σ_* relation for AGN and quiescent galaxies (red solid line). We distinguish between radio-loud quasars (RL QSO, blue circles) and radio-quiet quasars (RQ QSO, yellow circles). We now investigate which of these relations fits better to our RL and RQ QSO data when we fixed the slope, β, and leave the zero point, α, free. We search for the α parameter which provides the lowest dispersion between the observational points and these modified relationships for each case, and derive also the intrinsic scatter. Table 6 compiles our results, which are also plotted in Fig, 6. Interestingly, the M_{SMBH}-σ_* relation for AGN and quiescent galaxies provided by Woo et al. (2013) matches well our RQ QSO sample (both lines almost overlap in Fig, 6, as the best fit has α=8.26, being the scatter $\epsilon_0 = 0.511$), while the RL QSO sample is in better agreement with the relation for only AGN reported by these authors. In this case, we derive that an α=7.73 provides the best match between our observational points and the M_{SMBH}-σ_* relation for only AGN (cyan dotted line).

Table 6: Results of the fittings of our data sample, subdivided in RL and RQ QSO, when compared with the M_{SMBH}-σ_* relationships given by Woo et al. (2013) for AGN and AGN + quiescent galaxies.

	W13 AGN			W13 AGN+Q		
	α	β	ϵ_0	α	β	ϵ_0
W13 original	7.31	3.46	0.657	8.36	4.93	0.870
W13 fitted to RL	7.73	3.46	0.218	7.55	4.93	0.450
W13 original	7.31	3.46	1.144	8.36	4.93	0.603
W13 fitted to RQ	8.31	3.46	0.216	8.26	4.93	0.511

4.3. Comparing stellar velocity dispersions with FWHM of [O III]

As pointed out in the introduction, the FWHM of the [O III] λ5007 emission line has been used by some authors as a surrogate for stellar velocity dispersions (Nelson & Whittle 1996). In particular, Shields et al. (2003) used σ([O III] λ5007) and not σ_* to explore the M_{SMBH}-σ relation, finding a relatively large scatter.

We have compared the stellar velocity dis-

persions estimated for our sample quasars by Wolf & Sheinis (2008) with the velocity dispersion of the (narrow) [O III] λ5007 emission line derived from our fits (see Table 3). Left panel of Fig. 7 compares both velocity dispersions. From this Figure, it is evident that the assumption of using the velocity dispersion of the narrow [O III] λ5007 emission line as surrogate for σ_* is not satisfied. Actually, σ([O III] λ5007) seems to be completely independent of σ_*, particularly for low values.

We further investigate this issue in right panel of Fig. 7, where we plot the M_{SMBH}-σ relation using σ([O III] λ5007) instead of σ_*. This figure includes the data points compiled by Shields et al. (2003) –which are subdivided in RQ and RL AGN–, as well as the Tremaine et al. (2002) relation. We do not see any correlation at all between the position of our data with the position of the other objects and the relation. Indeed, the Tremaine et al. (2002) relation is valid for only one object. Again, the situation is particularly poor at the low-end of σ. We therefore conclude that σ([O III] λ5007) should not be used as a surrogate for stellar velocity dispersions for high-mass, high-luminosity quasars.

4.4. Comparing QSO radio-luminosities with SMBH masses

Nelson & Whittle (1996) reported a rather tight correlation between σ_* and radio luminosity in Seyfert galaxies, linking directly observable AGN properties to host galaxy properties. Given the subsequent $M_{\rm SMBH}$–σ_* correlation, one would expect to see a similar correlation between $M_{\rm SMBH}$ and radio luminosity. Such a correlation was reported by Franceschini, Vercellone, & Fabian (1998) for a small sample of 8 nearby early-type galaxies with black hole masses determined from stellar and gas dynamical studies. Later work with more galaxies, both quiescent and active, have shown much larger scatter or no correlation at all (Laor 2000; Ho 2002; Snellen et al. 2003; Woo et al. 2005). In fact, a bimodality in radio loudness as a function of M_{SMBH} has been suggested (Laor 2000).

Left panel of Fig. 8 compares the 5 GHz radio-continuum luminosity, $L_{5\,\rm GHz}$, of the quasar host galaxy with the derived SMBH masses. The radio data have been extracted from Wold et al. (2010), who estimated $L_{5\,\rm GHz}$ from previous literature data listed in the NED assuming a spectral index $\alpha = -5$. The limit between RL and RQ quasars –as given by $L_{5\,\rm GHz} \gtrsim 10^{41.5}\,{\rm erg\,s^{-1}}$ following Wold et al. (2010)– is shown in Fig. 8 with a dotted line. Following this figure, we see that RL QSO are found in our entire mass range, including in the low-mass limit –PKS 0736+017, which has $\log(M_{\rm SMBH}/M_\odot) = 7.67\pm0.04$–. As shown in the left panel of Fig. 8 a correlation between radio loudness and M_{SMBH} is not found in this mass range.

Conversely, the right panel of of Fig. 8 compares $L_{5\,\rm GHz}$, with the stellar velocity dispersion of the host galaxy. In this case, we observe a trend that galaxies with larger stellar velocity dispersion have larger 5 GHz radio-continuum luminosities. The red dashed line in this panel represents a linear fit to our data, in the form $\log(L_{5\,\rm GHz}) = A + B\log(\sigma_*)$, for which we derive $A = -23.3 \pm 19.0$, $B = 26.6 \pm 7.7$. The correlation coefficient is r=0.555.

4.5. Gas-phase metallicity of the host galaxies

We now use the fitted narrow emission lines to estimate the gas-phase metallicity of the host galaxies. Caution must be taken when attempting to do this, as the physical conditions that are responsible of the ionization of the gas are very different in H II regions and AGNs. The NLR spectrum is also a function of radiation pressure and, most important, the form of the extreme ultraviolet spectrum. Therefore photoionization models need to be considered to quantitatively derive metallicities in AGN hosts as the typical and very easy-to-apply empirical calibrations involving bright emission-lines used for computing metallicities in H II regions cannot be applied (e.g., Storchi Bergmann & Pastoriza 1989; Storchi-Bergmann et al. 1998; Hamann et al. 2002; Groves, Heckman & Kauffmann 2006; Husemann et al. 2014; Dopita et al. 2014).

We first check that the nature of the ionization of the narrow lines is massive stars (i.e., the narrow lines are produced in star-forming regions) using the [O III] λ5007/Hβ versus [N II] λ6583/Hα diagnostic diagram (Baldwin, Phillips & Terlevich 1981; Veilleux & Osterbrock 1987). This diagram is plotted in Fig. 9, and includes the analytic relations given by Dopita et al. (2000) and

TABLE 7

OXYGEN ABUNDANCES OF THE HOST GALAXIES USING THE NARROW LINES OBTAINED IN THE FIT OF OUR SPECTRA.

Object	[N II] λ6583/Hα	[O III] λ5007/Hβ	$N2$	$O3N2$	BPT	12 + log (O/H)			
						PP04 ($N2$)	PP04 ($O3N2$)	S-B98	Adopted
PG 0052+251	···	7.85	···	···	AGN?	···	···	···	···
PHL 909	···	11.4	···	···	AGN?	···	···	···	···
PKS 0736+017	···	1.27	···	···	H II?	···	···	···	···
3C 273	0.0116	0.208	-1.936	1.254	H II?	7.80	8.33	8.34	8.3[a]
PKS 1302-102	0.370	2.74	-0.870	0.907	H II	8.65	8.44	8.43	8.55 ± 0.10
PG 1309+355	···	3.53	···	···	H II?	···	···	···	8.48?[b]
PG 1444+407	···	0.180	···	···	H II?	···	···	···	···
PKS 2135-147	0.306	11.1	-0.514	1.560	AGN	8.61	8.23	8.57	8.3 – 8.6
4C 31.63	0.893	3.97	-0.0491	0.648	AGN	8.87	8.52	8.56	8.5 – 8.7
PKS 2349-014	0.839	4.70	-0.0762	0.748	AGN	8.86	8.49	8.56	8.5 – 8.7

[a]The derived value for [N II] λ6583 is extremely low. Although its position agrees with that expected for H II regions, another ionization mechanism is in action. We then consider the oxygen abundance provided by S-B98 calibration as tentative value for the metallicity of this object. See text for details.

[b]Tentative value considering the oxygen abundance given by the empirical calibration provided by Pilyugin (2001a,b), which considers the $R23$ and P parameters.

Kewley et al. (2001), as well as the empirical relation provided by Kauffmann et al. (2003a). The narrow lines derived in 4C 31.63, PKS 2135-147, and PKS 2349-014 (red circles) are still too broad to be produced only for photoionization by massive stars, as these objects do not lie in the loci of the H II regions in the diagnostic diagram. Hence, other mechanisms, as doppler broadening, outflows, or jet interactions, are playing an important role in the ionization of the lines. Thus, as shown in Fig. 9 we expect that photoionization by massive stars is the main excitation mechanism of the narrow lines in 3C 273 and PKS 1302-102 (blue circles). However, the faintness of the [N II] λ6583 line in 3C 273 moves this datapoint too far for what expected for an H II region, and hence other mechanisms are affecting the ionization of the narrow lines.

Purple triangles in Fig. 9 indicate the [O III] λ5007/Hβ position of objects for which [N II] λ6583/Hα is unknown (i.e., their true x-position on this diagram is not known). In the cases of PG 0052+251 and PHL 909, the high [O III] λ5007/Hβ value suggests that these objects do not lie in the loci of H II regions but in the AGN regime (if not, their metallicities should be very low, see Sánchez et al. 2014). On the other hand, the true position of PG 1444+407 –which has the lowest [O III] λ5007/Hβ ratio in our sample– in the BPT diagram shown in Fig. 9 may be close to the analytic relations plotted in this figure and therefore consistent with H II regions. The true position of objects PG 1309+355 and PKS 0736+017 in the BPT diagram may be consistent with H II regions (in the case $N2 \lesssim -0.8$ and -0.5, respectively) or LINERs (low-ionization narrow-emission line regions).

As mentioned above, for PKS 1302-102 the ionization of the narrow lines is massive stars. Therefore we can derive its oxygen abundance – in units of 12+log(O/H)– assuming the standard empirical calibrations to derive the metallicity in H II regions. We use the narrow lines of our fits and apply the standard empirical calibrations obtained by Pettini & Pagel (2004), which consider the $N2$ = log([N II] λ6583/Hα) and $O3N2$ = log{([O III] λ5007/Hβ) / ([N II] λ6583/Hα)} parameters. Table 7 compiles the results of the oxygen abundances obtained following these calibrations and the values of the $N2$ and $O3N2$ parameters when available. However, we note that caution must be taken when using empirical calibrations to derive the oxygen abundance in galaxies (see López-Sánchez et al. 2012, for a recent review about this topic). With this, we derive an oxygen abundance of 8.55±0.10 for PKS 1302-102. This value is the average oxygen abundance provided by these two empirical calibrations.

The spectrum of PG 1309+355 shows the nar-

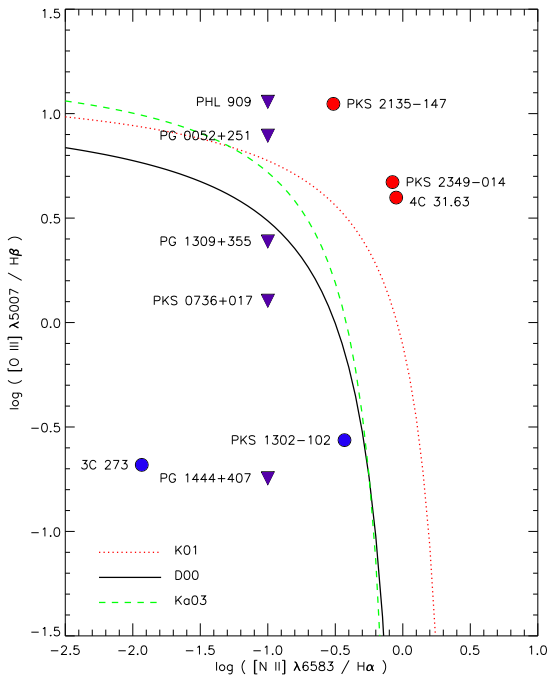

Fig. 9.— [O III] λ5007/Hβ versus [N II] λ6583/Hα diagnostic diagram for the ionized emission coming from the narrow components of our fits. The loci of the H II regions as proposed by Dopita et al. (2000), black continuous line (D00), Kewley et al. (2001), red dotted line (K01), and the empirical relation provided by Kauffmann et al. (2003a), dashed green line (Ka03), are also plotted. Circles indicate quasars for which both [O III] λ5007/Hβ and [N II] λ6583/Hα have been measured. In this case, only the narrow components of 3C 273 and PKS 1302-102 (blue circles) are expected to come from photoionization by massive stars, but an important shock contribution is expected in 4C 31.63, PKS 2135-147, and PK 2349-014 (red circles). However, the position of 3C 273 is too far for what expected from H II regions. Purple triangles indicate the [O III] λ5007/Hβ position of objects for which [N II] λ6583/Hα is unknown.

row [O II] λ3727 emission line. Assuming that the photoionization of the gas is coming from massive stars (as implied by Fig. 9), we can apply the empirical calibrations given by Pilyugin (2001a,b) –which consider the $R23$ and P parameters, defined as R_3 = ([O III] λ4959 + [O III] λ5007)/Hβ, R_2 = [O II] λ3727/Hβ, $R_{23} = R_3 + R_2$, and $P = R_3/R_{23}$– to get an estimation of the oxygen abundance of the ionized gas. We consider the Cardelli, Clayton & Mathis (1989) extinction law and assumed a reddening coefficient of c(Hβ)=0.4 to correct the [O II] λ3727 flux for reddening. With this, we derive f([O II] λ3727)/f(Hβ) = 0.343, $R23$=46.383, P=0.722, and 12+log(O/H)=8.48 for this object.

Storchi-Bergmann et al. (1998) computed the oxygen abundances for an artificial grid of line ratios with the photoionization code CLOUDY (Ferland et al. 1998) using an empirical AGN spectrum for the ionizing source. Storchi-Bergmann et al. (1998) also provided a calibration based on the ([O III] $\lambda\lambda$4959,5007)/Hβ and ([N II] $\lambda\lambda$6548,6583)/Hα line ratios by fitting a two-dimensional polynomial of second order to their grid of oxygen abundances. We use this calibration to get an estimation of the metallicity in 3C 273, 4C 31.63, PKS 2135-147, and PKS 2349-014. The results are also listed in Table 7. In all four cases we found 12+log(O/H) values between 8.3 and 8.6. As applying the Pettini & Pagel (2004) $N2$ calibration in AGNs will provide higher oxygen abundances than their true value, their results can be considered upper limits to the real metallicity of these objects. Hence, 4C 31.63, PKS 2135-147, and PKS 2349-014 seem to have oxygen abundances between 8.3 and 8.7. For the case of 3C 273, only the Storchi-Bergmann et al. (1998) equation can be used, we provide a tentative value of 12+log(O/H)$\sim$8.3 for its oxygen abundance. Although its real value may be slightly higher, the metallicity of 3C 273 is definitively subsolar.

These are the first attempt of deriving the gas-phase oxygen abundance in these quasars we are aware of. It is challenging to derive the oxygen abundances in active galaxies due to the strong contamination of the broad emission lines created by the AGN activity. However, detailed analyses indicate that most AGN tend to have solar –12+log(O/H)$_\odot$=8.69, Asplund et al. (2009)– to supersolar metallicities (Storchi Bergmann & Pastoriza 1989; Storchi-Bergmann et al. 1998; Hamann et al. 2002), reinforcing the hypothesis that AGN are usually found at high metallicities. Recently, Husemann et al. (2014) used the narrow emission lines to estimate the oxygen abundances of 11 low redshift ($z < 0.2$) quasar host galaxies,

all of them ranging between 8.5 and 9.0 (in the T_e-based absolute scale). Conversely, only few galaxies hosting AGN are found to have sub-solar metallicities, having in all cases masses lower than $10^{10}\,M_{\odot}$ (e.g., Groves, Heckman, & Kauffmann 2006; Barth, Greene, & Ho 2008; Izotov, Thuan, & Guseva 2007). In particular, out of a sample of ∼23000 Seyfert 2 galaxies, Groves, Heckman & Kauffmann (2006) found only ∼40 clear clear candidates for AGN with NLR abundances that are below solar. Low-metallicity AGN seem to be extremely rare (Izotov & Thuan 2008; Izotov et al. 2010). Hence, it is interesting to note that the oxygen abundances derived for our quasar sample are in the subsolar regime (metallicities between 0.4 $Z_{\odot}$ and $Z_{\odot}$). This may suggest that low-z, higher luminosity quasars have higher probability of being found in subsolar metallicity hosts than low-luminosity quasars. This is a reasonable argument, as brighter AGNs are expected to consume more gas, suggesting these AGNs are found in host galaxies with large gas reservoirs, and hence lower metallicity as the gas has not yet been primarily processed into stars.

4.6. On the nature of the RL and RQ quasars

Is there a true physical difference between RL and RQ quasars beyond their radio luminosity? Laor (2000) found that virtually all of the RL quasars contain SMBH with masses $M_{\rm SMBH} > 10^9 M_{\odot}$, whereas the majority of the RQ quasars host a SMBH with masses $M_{\rm SMBH} < 3 \times 10^8 M_{\odot}$. Lacy et al. (2001) established that a continuous variation of radio luminosity with BH mass existed and that the radio power also depends on the accretion rate relative to the Eddington limit. Later, McLure & Dunlop (2002) found a similar result, quantifying that the median BH mass of the RL quasars are a factor 2 larger than that of their RQ counterparts. However, Ho (2002) and Jarvis & McLure (2002) found no clear relationship between radio power and black hole mass. McLure & Jarvis (2004) used a sample of more than 6000 quasars from SDSS to find that RL quasars are found to harbour systematically more massive black holes than are the RQ quasars. These authors also reported a strong correlation between radio luminosity and SMBH mass.

RQ quasars seem to be associated with mixed morphologies including spiral galaxies, as they tend to have lower σ_* than RL quasars (Wolf & Sheinis 2008). Recently Kimball et al. (2011) used the Expanded Very Large Array (EVLA) to observe at 6 GHz 179 quasars in the redshift range $0.2 < z < 0.3$, detecting 97% of them. These authors concluded that the radio luminosity function is consistent with the hypothesis that the radio emission in RL quasars is powered primary by AGNs, while the radio emission in RQ quasars is powered primarily by star-formation in their host galaxies (i.e., their host galaxies are spiral galaxies).

Although we consider only the study of 10 objects, our analysis appears to agree with Kimball et al. (2011) conclusions, as it suggests that the M_{SMBH}-σ_* relation of RQ quasars matches well with that found in AGN+quiescent galaxies (i.e., still star-forming galaxies) and that the M_{SMBH}-σ_* relation of RL quasars follows that found only in AGN. Indeed, stellar population synthesis analyses of quasars have shown that the radio-luminosity of RQ quasars is consistent with that found in quiescent star-forming galaxies (Wold et al. 2010). Following our analysis, PG 1309+355, a RQ quasar, also seems to show a relatively important star-formation activity. The importance of the star-formation activity in the quasar host galaxy may be just another consequence of whatever physical phenomenon is responsible for its RL or RQ nature.

As presented in Wolf & Sheinis (2008), we hypothesize that RQ quasars may be formed by a more secular merger scenario than RL quasars, in that many RL quasars show signs of recent or ongoing interactions including major merger events (Zakamska et al. 2006; Villar-Martín et al. 2011, 2012; Bessiere et al. 2012; Villar-Martín et al. 2013). Low surface brightness fine structure indicate of past merger events can easily be missed if too shallow images are used (e.g. Bennert et al. 2008, and references within). However Ramos Almeida et al. (2012) recently found that ∼95% of their radio-loud AGN host show interaction signatures, and suggested that radio-loud quasars are also triggered by interactions. In the case or RQ quasars, the merger scenario appears much more rare and may point to RL quasars likely occurring in harassment and minor merger events (whose features can be dif-

ficult to detect even in deep images). If this is the case, it is also possible that the major mergers are more likely to lead to binary black holes (Begelman, Blandford & Rees 1980; Roos 1981; Khan, Just & Merritt 2011) as the BH mass scales with galaxy mass while RQ quasars events are characterize by minor mergers in which only a single BH survives due to the mass disparity. The merger of two SMBH seems to be the most plausible scenario to explain the X-shaped morphology observed in some bright radio-galaxies (Merritt & Ekers 2002; Hodges-Kluck et al. 2010; Gong, Li & Zhang 2011; Mezcua et al. 2011, 2012). The scenario where the AGNs radio luminosity is fueled by binary BH activity is consistent with our host galaxy observations (RL hosts tend to be more massive than RQ hosts, Wolf & Sheinis 2008), with the observational result that RL quasars harbour systematically more massive black holes than the RQ quasars (McLure & Dunlop 2002; McLure & Jarvis 2004), as well as the observation by Kimball et al. (2011) that show the radio luminosity of the stellar component of the galaxy is a much smaller contribution to the total radio luminosity on RL quasars. These ideas require further exploration.

5. Conclusions

We have analyzed the emission line profiles of a sample of 10 quasars and derive their supermassive black hole masses following the virial method. Our sample consists in 6 radio-loud quasars and 4 radio-quiet quasars. We carefully fit a broad and narrow Gaussian component for each bright emission line in both the Hβ (10 objects) and Hα regions (5 objects). Our main conclusions are:

1. We find a very good agreement of the derived SMBH masses, $M_{\rm SMBH}$, using the fitted broad Hβ and Hα emission lines. We compare our $M_{\rm SMBH}$ results with those found by previous studies using the reverberation mapping technique, the virial method and X-ray data, as well as those derived using the continuum luminosity at 5100 Å.

2. We study the relationship between the $M_{\rm SMBH}$ of the quasar and the stellar velocity dispersion, σ_*, of the host galaxy. We use the measured $M_{\rm SMBH}$ and σ_* to investigate the $M_{\rm SMBH}$ – σ_* relation for both the radio-loud and radio-quiet subsamples. Besides the scatter and the low number of objects in our sample, we find a good agreement between radio-quiet quasars and AGN+quiescent galaxies and between radio-loud quasars and AGN. The intercept in the latter case is 0.5 dex lower than in the first case. Our results support the idea that both the star-formation phenomena in the host galaxy and the RL or RQ nature of the quasar are a consequence of a different merger scenario, possibly being RL quasars triggered by a major merger event and RQ quasars ignited by a minor merger event. Major mergers are more likely to lead to binary black holes, which inter-relationship may drastically enhance the radio activity.

3. Our analysis does not support the hypothesis of using σ([O III] λ5007) as a surrogate for stellar velocity dispersions in high-mass, high-luminosity quasars.

4. We also investigate the relationship between the 5 GHz radio-continuum luminosity, $L_{5\,\rm GHz}$, of the quasar host galaxy with both $M_{\rm SMBH}$ and σ_*. We do not find any correlation between $L_{5\,\rm GHz}$ and $M_{\rm SMBH}$, although we observe a trend that galaxies with larger stellar velocity dispersions have larger 5 GHz radio-continuum luminosities.

5. Using the results of our fitting for the narrow emission lines of [O III] λ5007 and [N II] λ6583 we estimate the gas-phase oxygen abundance of six quasars, being subsolar in all cases. These are the first attempt of deriving the gas-phase oxygen abundance in these quasars we know of. We suggest that low-z, higher luminosity quasars have higher probability of being found in subsolar metallicity hosts than low-luminosity quasars, as the latter have probably processed more gas into stars than high-luminosity quasars.

We are indebted to Marsha Wolf for her discussions and data reduction comments on the σ_* . We are grateful to Scott Croom, Paul Martini,

César Esteban and Mike Dopita for providing their very valuable comments to this work and to Joe Miller who provided the original impetus for this research. We also thank Louis Ho for the early discussions motivating this work. This research has made use of the SAO/NASA Astrophysics Data System Bibliographic Services (ADS). This research has made extensive use of the NASA/IPAC Extragalactic Database (NED) which is operated by the Jet Propulsion Laboratory, Caltech, under contract with the National Aeronautics and Space Administration.

REFERENCES

Asplund M., Grevesse N., Sauval A. J., Scott P., 2009, ARA&A, 47, 481

Assef R. J. et al., 2011, ApJ, 742, 93

Bahcall J. N., Kirhakos S., Saxe D. H., Schneider D. P., 1997, ApJ, 479, 642

Baldry I. K., Glazebrook K., Brinkmann J., Ivezić Ž., Lupton R. H., Nichol R. C., Szalay A. S., 2004, ApJ, 600, 681

Baldwin J. A., Phillips M. M., Terlevich R., 1981, PASP, 93, 5

Barth A. J., Greene J. E., Ho L. C., 2008, AJ, 136, 1179

Begelman M. C., Blandford R. D., Rees M. J., 1980, Nature, 287, 307

Bell E. F. et al., 2004, ApJ, 608, 752

Bennert N., Canalizo G., Jungwiert B., Stockton A., Schweizer F., Peng C. Y., Lacy M., 2008, ApJ, 677, 846

Bentz M. C. et al., 2013, ApJ, 767, 149

Bentz M. C. et al., 2010, ApJ, 720, L46

Bentz M. C., Peterson B. M., Netzer H., Pogge R. W., Vestergaard M., 2009a, ApJ, 697, 160

Bentz M. C., Peterson B. M., Pogge R. W., Vestergaard M., 2009b, ApJ, 694, L166

Bentz M. C., Peterson B. M., Pogge R. W., Vestergaard M., Onken C. A., 2006, ApJ, 644, 133

Bernardi M. et al., 2003, AJ, 125, 1882

Bershady M. A., Andersen D. R., Harker J., Ramsey L. W., Verheijen M. A. W., 2004, PASP, 116, 565

Bershady M. A., Andersen D. R., Verheijen M. A. W., Westfall K. B., Crawford S. M., Swaters R. A., 2005, ApJS, 156, 311

Bessiere P. S., Tadhunter C. N., Ramos Almeida C., Villar Martín M., 2012, MNRAS, 426, 276

Blandford R. D., McKee C. F., 1982, ApJ, 255, 419

Boroson T. A., Green R. F., 1992, ApJS, 80, 109

Bryant J. J. et al., 2015, MNRAS, 447, 2857

Cardelli J. A., Clayton G. C., Mathis J. S., 1989, ApJ, 345, 245

Cattaneo A., Dekel A., Devriendt J., Guiderdoni B., Blaizot J., 2006, MNRAS, 370, 1651

Cid Fernandes R., Mateus A., Sodré L., Stasińska G., Gomes J. M., 2005, MNRAS, 358, 363

Cimatti A. et al., 2002, A&A, 381, L68

Croom S. M. et al., 2012, MNRAS, 421, 872

Czerny B., Nikołajuk M., 2010, Mem. Soc. Astron. Italiana, 81, 281

Dasyra K. M. et al., 2007, ApJ, 657, 102

Decarli R., Labita M., Treves A., Falomo R., 2008, MNRAS, 387, 1237

Dekel A., Birnboim Y., 2006, MNRAS, 368, 2

Denney K. D., Peterson B. M., Dietrich M., Vestergaard M., Bentz M. C., 2009a, ApJ, 692, 246

Denney K. D., Peterson B. M., Dietrich M., Vestergaard M., Bentz M. C., 2009b, ApJ, 692, 246

Dopita M. A., Kewley L. J., Heisler C. A., Sutherland R. S., 2000, ApJ, 542, 224

Dopita M. A. et al., 2014, A&A, 566, A41

Drory N., Feulner G., Bender R., Botzler C. S., Hopp U., Maraston C., Mendes de Oliveira C., Snigula J., 2001, MNRAS, 325, 550

Dunlop J. S., McLure R. J., Kukula M. J., Baum S. A., O'Dea C. P., Hughes D. H., 2003, MNRAS, 340, 1095

Fabian A. C., 1999, MNRAS, 308, L39

Ferland G. J., Korista K. T., Verner D. A., Ferguson J. W., Kingdon J. B., Verner E. M., 1998, PASP, 110, 761

Ferrarese L., Merritt D., 2000, ApJ, 539, L9

Ferrarese L., Pogge R. W., Peterson B. M., Merritt D., Wandel A., Joseph C. L., 2001, ApJ, 555, L79

Fogarty L. M. R. et al., 2012, ApJ, 761, 169

Franceschini A., Vercellone S., Fabian A. C., 1998, MNRAS, 297, 817

Fu H., Stockton A., 2009, ApJ, 696, 1693

Gadotti D. A., Kauffmann G., 2009, MNRAS, 399, 621

García-Benito R. et al., 2015, A&A, 576, A135

García-Lorenzo B. et al., 2015, A&A, 573, A59

Gebhardt K. et al., 2000a, ApJ, 539, L13

Gebhardt K. et al., 2003, ApJ, 597, 239

Gebhardt K. et al., 2000b, ApJ, 543, L5

Ghosh K. K., Ramsey B. D., Sadun A. C., Soundararajaperumal S., 2000, ApJS, 127, 11

Giavalisco M. et al., 2004, ApJ, 600, L93

Gliozzi M., Titarchuk L., Satyapal S., Price D., Jang I., 2011, ApJ, 735, 16

Gong B. P., Li Y. P., Zhang H. C., 2011, ApJ, 734, L32

Graham A. W., 2008a, ApJ, 680, 143

Graham A. W., 2008b, PASA, 25, 167

Graham A. W., Li I.-h., 2009, ApJ, 698, 812

Graham A. W., Onken C. A., Athanassoula E., Combes F., 2011, MNRAS, 412, 2211

Greene J. E., Ho L. C., 2005, ApJ, 630, 122

Greene J. E., Ho L. C., Barth A. J., 2008, ApJ, 688, 159

Greene J. E. et al., 2010, ApJ, 721, 26

Grier C. J. et al., 2013, ApJ, 773, 90

Groves B. A., Heckman T. M., Kauffmann G., 2006, MNRAS, 371, 1559

Gültekin K. et al., 2009, ApJ, 698, 198

Guyon O., Sanders D. B., Stockton A., 2006, ApJS, 166, 89

Hamann F., Korista K. T., Ferland G. J., Warner C., Baldwin J., 2002, ApJ, 564, 592

Heavens A., Panter B., Jimenez R., Dunlop J., 2004, Nature, 428, 625

Ho I.-T. et al., 2014, MNRAS, 444, 3894

Ho L., 1999, in Astrophysics and Space Science Library, Vol. 234, Observational Evidence for the Black Holes in the Universe, Chakrabarti S. K., ed., p. 157

Ho L. C., 2002, ApJ, 564, 120

Hodges-Kluck E. J., Reynolds C. S., Miller M. C., Cheung C. C., 2010, ApJ, 717, L37

Hogg D. W. et al., 2003, ApJ, 585, L5

Holt J., Tadhunter C. N., Morganti R., 2008, MNRAS, 387, 639

Hooimeyer J. R. A., Miley G. K., de Waard G. J., Schilizzi R. T., 1992, A&A, 261, 9

Hu C., Wang J.-M., Ho L. C., Chen Y.-M., Bian W.-H., Xue S.-J., 2008, ApJ, 683, L115

Husemann B., Jahnke K., Sánchez S. F., Wisotzki L., Nugroho D., Kupko D., Schramm M., 2014, MNRAS, 443, 755

Izotov Y. I., Guseva N. G., Fricke K. J., Stasińska G., Henkel C., Papaderos P., 2010, A&A, 517, A90

Izotov Y. I., Thuan T. X., 2008, ApJ, 687, 133

Izotov Y. I., Thuan T. X., Guseva N. G., 2007, ApJ, 671, 1297

Jarvis M. J., McLure R. J., 2002, MNRAS, 336, L38

Jorgensen I., Franx M., Kjaergaard P., 1995, MNRAS, 276, 1341

Kang W.-R., Woo J.-H., Schulze A., Riechers D. A., Kim S. C., Park D., Smolcic V., 2013, ApJ, 767, 26

Kaspi S., Maoz D., Netzer H., Peterson B. M., Vestergaard M., Jannuzi B. T., 2005, ApJ, 629, 61

Kaspi S., Smith P. S., Netzer H., Maoz D., Jannuzi B. T., Giveon U., 2000, ApJ, 533, 631

Kauffmann G. et al., 2003a, MNRAS, 346, 1055

Kauffmann G. et al., 2003b, MNRAS, 341, 54

Kewley L. J., Dopita M. A., Sutherland R. S., Heisler C. A., Trevena J., 2001, ApJ, 556, 121

Khan F. M., Just A., Merritt D., 2011, ApJ, 732, 89

Kim M., Ho L. C., Peng C. Y., Barth A. J., Im M., Martini P., Nelson C. H., 2008, ApJ, 687, 767

Kimball A. E., Kellermann K. I., Condon J. J., Ivezić Ž., Perley R. A., 2011, ApJ, 739, L29

King A. R., 2010, MNRAS, 408, L95

Koo D. C. et al., 2005, ApJS, 157, 175

Kormendy J., Bender R., Cornell M. E., 2011, Nature, 469, 374

Kormendy J., Gebhardt K., Richstone D., 2000, in Bulletin of the American Astronomical Society, Vol. 32, American Astronomical Society Meeting Abstracts #196, p. 702

Kormendy J., Richstone D., 1995, ARA&A, 33, 581

Krolik J. H., 2001, ApJ, 551, 72

Labbé I. et al., 2003, AJ, 125, 1107

Lacy M., Laurent-Muehleisen S. A., Ridgway S. E., Becker R. H., White R. L., 2001, ApJ, 551, L17

Laor A., 2000, ApJ, 543, L111

Liu G., Zakamska N. L., Greene J. E., Nesvadba N. P. H., Liu X., 2013a, MNRAS, 430, 2327

Liu G., Zakamska N. L., Greene J. E., Nesvadba N. P. H., Liu X., 2013b, MNRAS, 436, 2576

Lloyd C., 1984, MNRAS, 209, 697

López-Sánchez Á. R., Dopita M. A., Kewley L. J., Zahid H. J., Nicholls D. C., Scharwächter J., 2012, MNRAS, 426, 2630

Mathur S., Fields D., Peterson B. M., Grupe D., 2012, ApJ, 754, 146

McCarthy P. J. et al., 2004, ApJ, 614, L9

McConnell N. J., Ma C.-P., 2013, ApJ, 764, 184

McConnell N. J., Ma C.-P., Gebhardt K., Wright S. A., Murphy J. D., Lauer T. R., Graham J. R., Richstone D. O., 2011, Nature, 480, 215

McGill K. L., Woo J.-H., Treu T., Malkan M. A., 2008, ApJ, 673, 703

McLure R. J., Dunlop J. S., 2002, MNRAS, 331, 795

McLure R. J., Jarvis M. J., 2002, MNRAS, 337, 109

McLure R. J., Jarvis M. J., 2004, MNRAS, 353, L45

Merritt D., Ekers R. D., 2002, Science, 297, 1310

Mezcua M., Chavushyan V. H., Lobanov A. P., León-Tavares J., 2012, A&A, 544, A36

Mezcua M., Lobanov A. P., Chavushyan V. H., León-Tavares J., 2011, A&A, 527, A38

Miller J. S., Sheinis A. I., 2003, ApJ, 588, L9

Nelson C. H., Green R. F., Bower G., Gebhardt K., Weistrop D., 2004, ApJ, 615, 652

Nelson C. H., Whittle M., 1996, ApJ, 465, 96

Nesvadba N. P. H., Lehnert M. D., Eisenhauer F., Gilbert A., Tecza M., Abuter R., 2006, ApJ, 650, 693

Oke J. B. et al., 1994, in Society of Photo-Optical Instrumentation Engineers (SPIE) Conference Series, Vol. 2198, Instrumentation in Astronomy VIII, Crawford D. L., Craine E. R., eds., pp. 178–184

Onken C. A., Ferrarese L., Merritt D., Peterson B. M., Pogge R. W., Vestergaard M., Wandel A., 2004, ApJ, 615, 645

Osterbrock D. E., Ferland G. J., 2006, Astrophysics of gaseous nebulae and active galactic nuclei. University Science Books, Sausalito, CA

Pancoast A., Brewer B. J., Treu T., 2014, MNRAS, 445, 3055

Park D., Kelly B. C., Woo J.-H., Treu T., 2012, ApJS, 203, 6

Peterson B. M., 2010, in IAU Symposium, Vol. 267, IAU Symposium, Peterson B. M., Somerville R. S., Storchi-Bergmann T., eds., pp. 151–160

Peterson B. M. et al., 2004, ApJ, 613, 682

Pettini M., Pagel B. E. J., 2004, MNRAS, 348, L59

Pilyugin L. S., 2001a, A&A, 369, 594

Pilyugin L. S., 2001b, A&A, 374, 412

Ramos Almeida C. et al., 2012, MNRAS, 419, 687

Roos N., 1981, A&A, 95, 349

Sánchez S. F. et al., 2012, A&A, 538, A8

Sánchez S. F. et al., 2015, A&A, 574, A47

Sánchez S. F. et al., 2014, ArXiv:1409.8293

Schlegel D. J., Finkbeiner D. P., Davis M., 1998, ApJ, 500, 525

Shaposhnikov N., Titarchuk L., 2009, ApJ, 699, 453

Sheinis A. I., 2002, PhD thesis, UC Santa Cruz

Shen Y., 2013, Bulletin of the Astronomical Society of India, 41, 61

Shen Y., Liu X., 2012, ApJ, 753, 125

Shields G. A., Gebhardt K., Salviander S., Wills B. J., Xie B., Brotherton M. S., Yuan J., Dietrich M., 2003, ApJ, 583, 124

Silk J., Rees M. J., 1998, A&A, 331, L1

Snellen I. A. G., Lehnert M. D., Bremer M. N., Schilizzi R. T., 2003, MNRAS, 342, 889

Soldi S. et al., 2008, A&A, 486, 411

Storchi Bergmann T., Pastoriza M. G., 1989, ApJ, 347, 195

Storchi-Bergmann T., Schmitt H. R., Calzetti D., Kinney A. L., 1998, AJ, 115, 909

Tremaine S. et al., 2002, ApJ, 574, 740

Veilleux S., Osterbrock D. E., 1987, ApJS, 63, 295

Véron-Cetty M.-P., Joly M., Véron P., 2004, A&A, 417, 515

Vestergaard M., Peterson B. M., 2006, ApJ, 641, 689

Villar-Martín M., Cabrera Lavers A., Bessiere P., Tadhunter C., Rose M., de Breuck C., 2012, MNRAS, 423, 80

Villar-Martín M., Emonts B., Rodríguez M., Torres M. P., Drouart G., 2013, MNRAS, 432, 2104

Villar-Martín M., Tadhunter C., Humphrey A., Encina R. F., Delgado R. G., Torres M. P., Martínez-Sansigre A., 2011, MNRAS, 416, 262

Wandel A., Peterson B. M., Malkan M. A., 1999, ApJ, 526, 579

Watson L. C., Martini P., Dasyra K. M., Bentz M. C., Ferrarese L., Peterson B. M., Pogge R. W., Tacconi L. J., 2008, ApJ, 682, L21

Wild V. et al., 2014, A&A, 567, A132

Wold I., Sheinis A. I., Wolf M. J., Hooper E. J., 2010, MNRAS, 408, 713

Wolf M. J., Sheinis A. I., 2008, AJ, 136, 1587

Woo J.-H., Schulze A., Park D., Kang W.-R., Kim S. C., Riechers D. A., 2013, ApJ, 772, 49

Woo J.-H. et al., 2010, ApJ, 716, 269

Woo J.-H., Urry C. M., van der Marel R. P., Lira P., Maza J., 2005, ApJ, 631, 762

Zakamska N. L., Greene J. E., 2014, MNRAS, 442, 784

Zakamska N. L. et al., 2006, AJ, 132, 1496

Zubovas K., King A. R., 2012, MNRAS, 426, 2751

6. Appendix

Figures 10 to 15 show the fit to the emission line profiles of the rest of our quasar sample, following the same conventions we specified in Figs. 1 and 2.

This 2-column preprint was prepared with the AAS LaTeX macros v5.2.

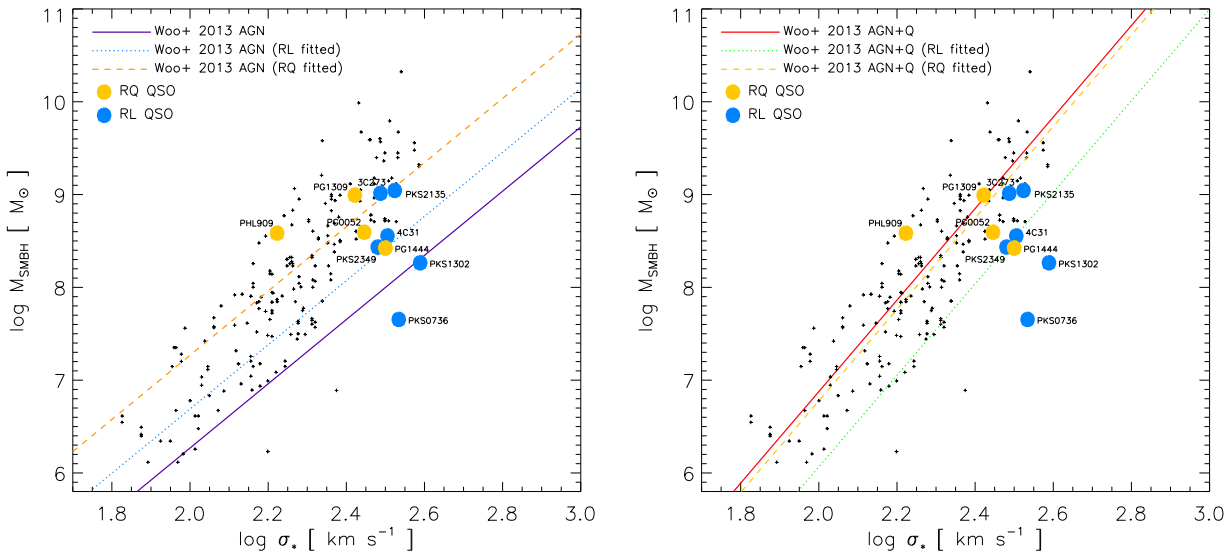

Fig. 6.— Comparison of our QSO sample datapoints with the new M_{SMBH}-σ_* relations provided by Woo et al. (2013). We consider the cases of only AGN (Left) and AGN + quiescent galaxies (Right) relations. QSO host galaxies from this work are shown as large circles (radio-loud are blue, radio-quiet are yellow). The black crosses represent all the previous data included in Fig. 5. The original M_{SMBH}-σ_* relationships are plotted with a purple (AGN) or red (AGN+quiescent) continuos line. The best fits to the Woo et al. (2013) M_{SMBH}-σ_* relation fixing the slope are plotted with a cyan dotted line (only for AGN and our RL QSO), an orange dashed line (only for AGN and our RQ QSO), a green dotted line (for AGN + quiescent galaxies and our RL QSO), and a dashed yellow line (for AGN + quiescent galaxies and our RQ QSO).

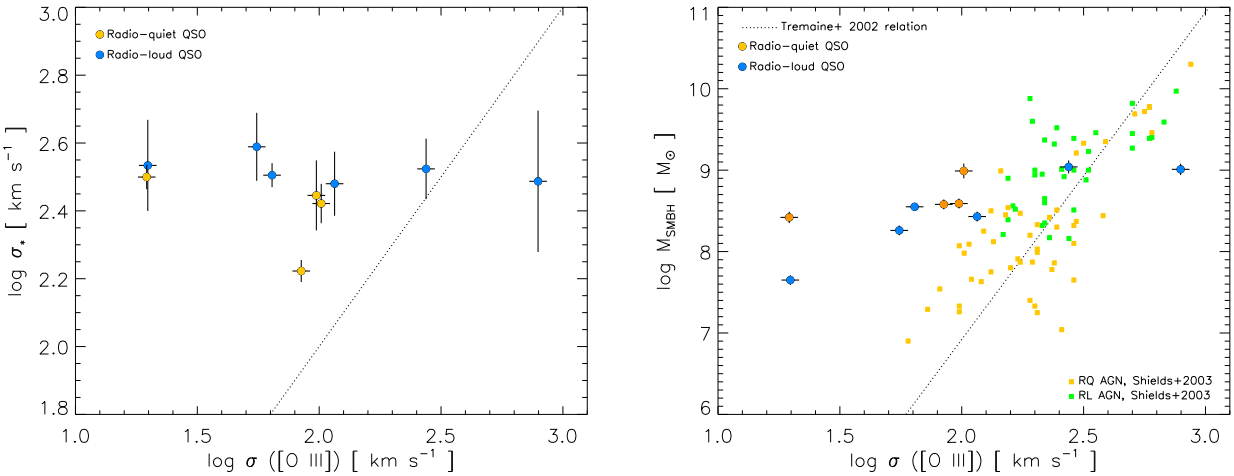
Radio−quiet QSO
Radio−loud QSO
log σ* [km s^-1]
log σ ([O III]) [km s^-1]
Tremaine+ 2002 relation
RQ AGN, Shields+2003
RL AGN, Shields+2003
log M_SMBH [M⊙]

Fig. 7.— (Left) Comparison between the stellar velocity dispersion, $\sigma_\star$, given by Wolf & Sheinis (2008), with the σ of the broad [O III] λ5007 emission line derived in our fitting. The dotted line represents $x = y$. (Right) The M_{SMBH}-σ relation using the σ of the narrow [O III] λ5007. AGN data points by Shields et al. (2003) are plotted with orange squares. In both panels radio-loud QSO are blue circles, radio-quiet QSO are yellow circles.

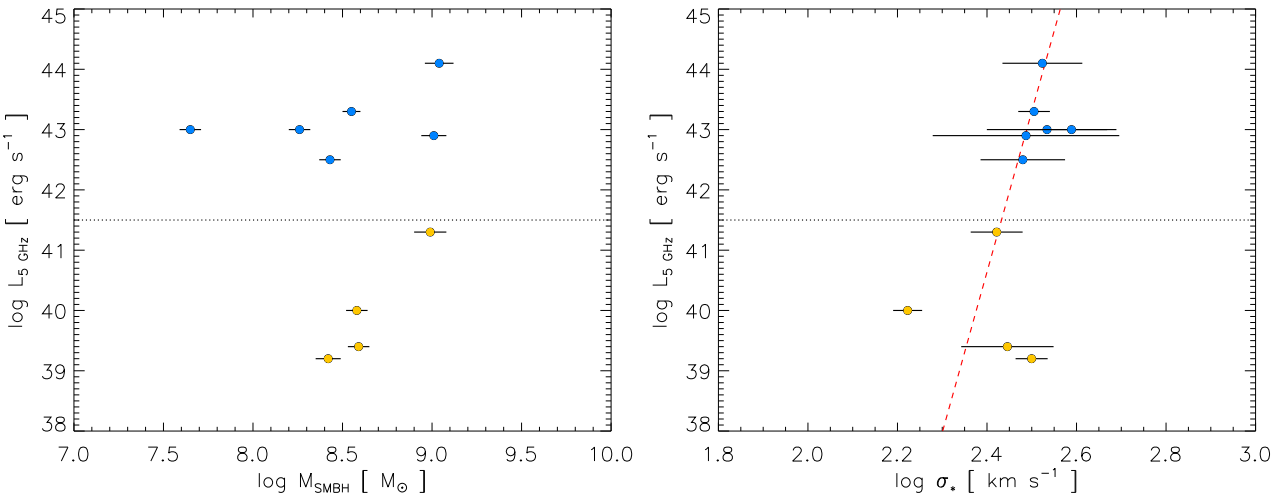

Fig. 8.— (Left panel) Comparison between the mass derived for the SMBH and the 5 GHz radio-luminosity of the host galaxy, as given by Wold et al. (2010). (Right panel) Comparison between the stellar velocity dispersion of the galaxy hosting a QSO –given by Wolf & Sheinis (2008)– and its 5 GHz radio-luminosity –given by Wold et al. (2010)–. In both panels, radio-loud QSO are blue circles, radio-quiet QSO are yellow circles. We include the limit between RL and RQ quasars as given by $L_{5\,\mathrm{GHz}} \gtrsim 10^{41.5}\,\mathrm{erg\,s^{-1}}$ (Wold et al. 2010). Red dashed line in right panel represents a linear fit to our data

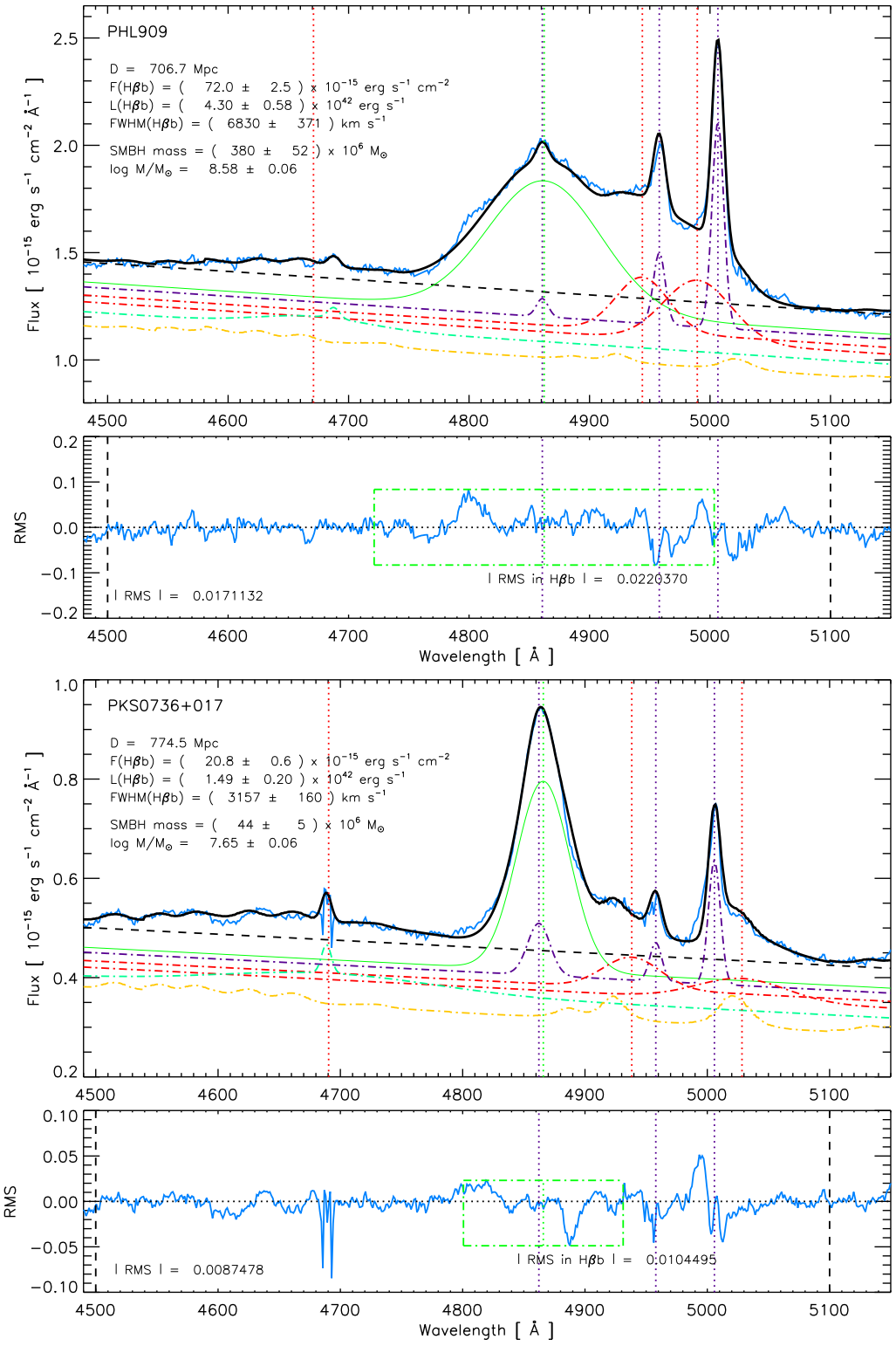
PHL909
D = 706.7 Mpc
F(Hβb) = (72.0 ± 2.5) x 10^-15 erg s^-1 cm^-2
L(Hβb) = (4.30 ± 0.58) x 10^42 erg s^-1
FWHM(Hβb) = (6830 ± 371) km s^-1
SMBH mass = (380 ± 52) x 10^6 M⊙
log M/M⊙ = 8.58 ± 0.06
Flux [10^-15 erg s^-1 cm^-2 Å^-1]
RMS
| RMS | = 0.0171132
| RMS in Hβb | = 0.0220370
Wavelength [Å]
PKS0736+017
D = 774.5 Mpc
F(Hβb) = (20.8 ± 0.6) x 10^-15 erg s^-1 cm^-2
L(Hβb) = (1.49 ± 0.20) x 10^42 erg s^-1
FWHM(Hβb) = (3157 ± 160) km s^-1
SMBH mass = (44 ± 5) x 10^6 M⊙
log M/M⊙ = 7.65 ± 0.06
Flux [10^-15 erg s^-1 cm^-2 Å^-1]
RMS
| RMS | = 0.0087478
| RMS in Hβb | = 0.0104495
Wavelength [Å]

Fig. 10.— Fit to the emission line profiles of PHL 909 and PKS 0736+017 around the Hβ region. The lines are the same described in Fig. 1.

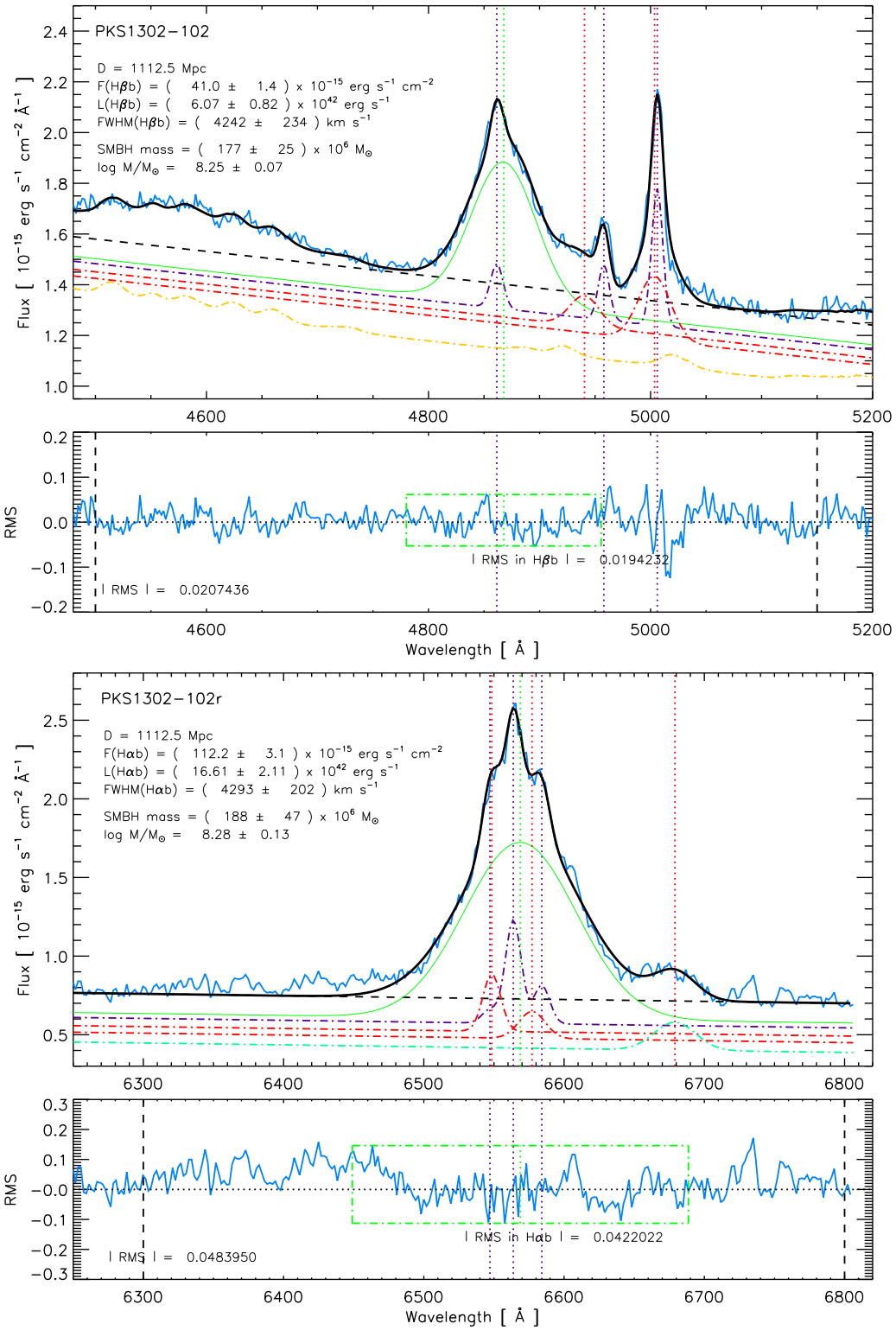
PKS1302−102
D = 1112.5 Mpc
F(Hβb) = (41.0 ± 1.4) x 10^-15 erg s^-1 cm^-2
L(Hβb) = (6.07 ± 0.82) x 10^42 erg s^-1
FWHM(Hβb) = (4242 ± 234) km s^-1
SMBH mass = (177 ± 25) x 10^6 M⊙
log M/M⊙ = 8.25 ± 0.07
Flux [10^-15 erg s^-1 cm^-2 Å^-1]
RMS
| RMS in Hβb | = 0.0194232
| RMS | = 0.0207436
Wavelength [Å]
PKS1302−102r
D = 1112.5 Mpc
F(Hαb) = (112.2 ± 3.1) x 10^-15 erg s^-1 cm^-2
L(Hαb) = (16.61 ± 2.11) x 10^42 erg s^-1
FWHM(Hαb) = (4293 ± 202) km s^-1
SMBH mass = (188 ± 47) x 10^6 M⊙
log M/M⊙ = 8.28 ± 0.13
Flux [10^-15 erg s^-1 cm^-2 Å^-1]
RMS
| RMS in Hαb | = 0.0422022
| RMS | = 0.0483950
Wavelength [Å]

Fig. 11.— Fit to the emission line profiles of PKS 1302-102 around the Hβ region (top) and the Hα region (bottom). The lines are the same described in Fig. 1, following the same procedure for Hα as described in Fig. 2.

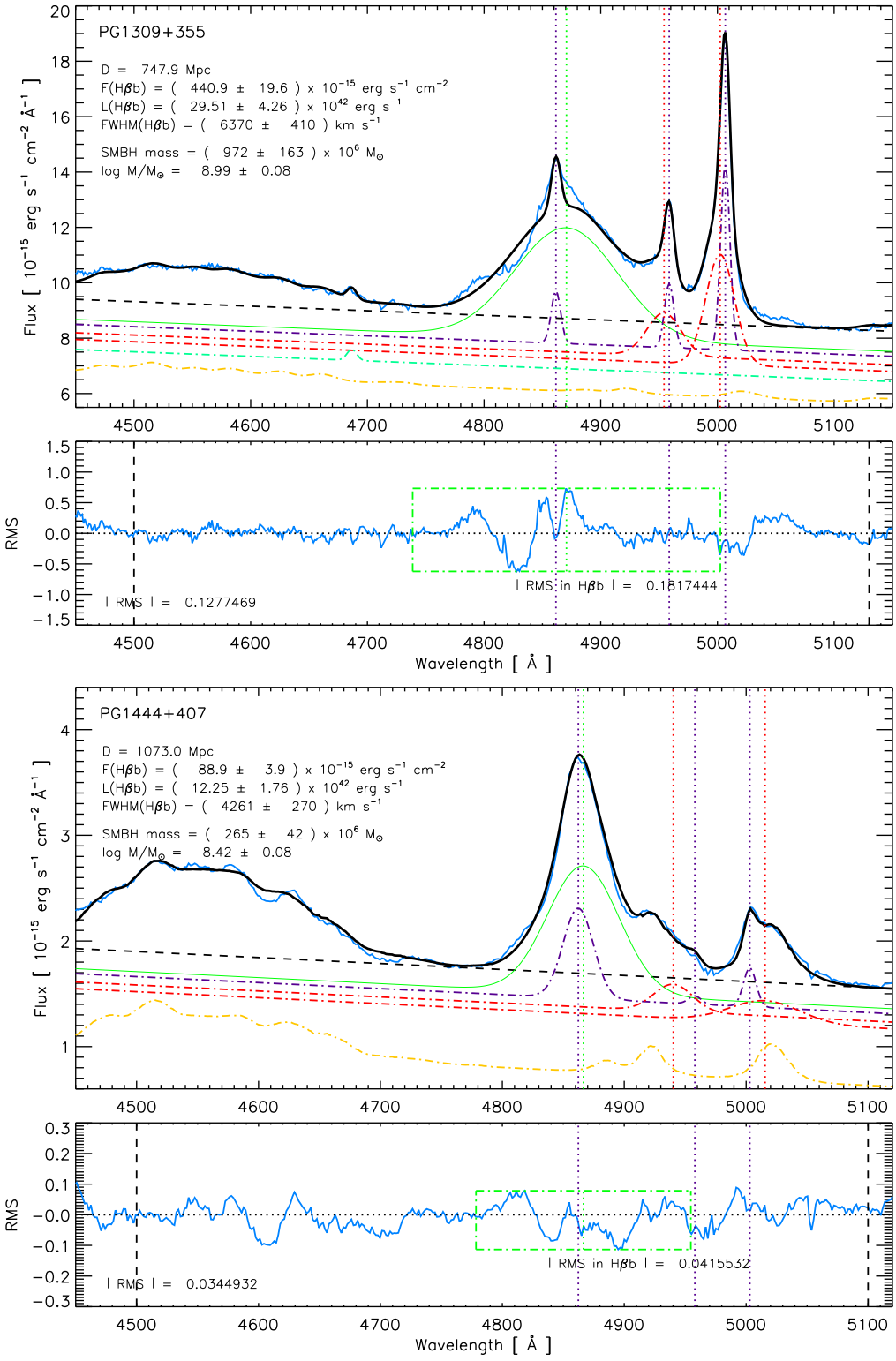
PG1309+355
D = 747.9 Mpc
F(Hβb) = (440.9 ± 19.6) x 10^-15 erg s^-1 cm^-2
L(Hβb) = (29.51 ± 4.26) x 10^42 erg s^-1
FWHM(Hβb) = (6370 ± 410) km s^-1
SMBH mass = (972 ± 163) x 10^6 M⊙
log M/M⊙ = 8.99 ± 0.08
Flux [10^-15 erg s^-1 cm^-2 Å^-1]
RMS
| RMS | = 0.1277469
| RMS in Hβb | = 0.1817444
Wavelength [Å]
PG1444+407
D = 1073.0 Mpc
F(Hβb) = (88.9 ± 3.9) x 10^-15 erg s^-1 cm^-2
L(Hβb) = (12.25 ± 1.76) x 10^42 erg s^-1
FWHM(Hβb) = (4261 ± 270) km s^-1
SMBH mass = (265 ± 42) x 10^6 M⊙
log M/M⊙ = 8.42 ± 0.08
Flux [10^-15 erg s^-1 cm^-2 Å^-1]
RMS
| RMS | = 0.0344932
| RMS in Hβb | = 0.0415532
Wavelength [Å]

Fig. 12.— Fit to the emission line profiles of PG 1309+355 and PG 1444+407 around the Hβ region. The lines are the same described in Fig. 1.

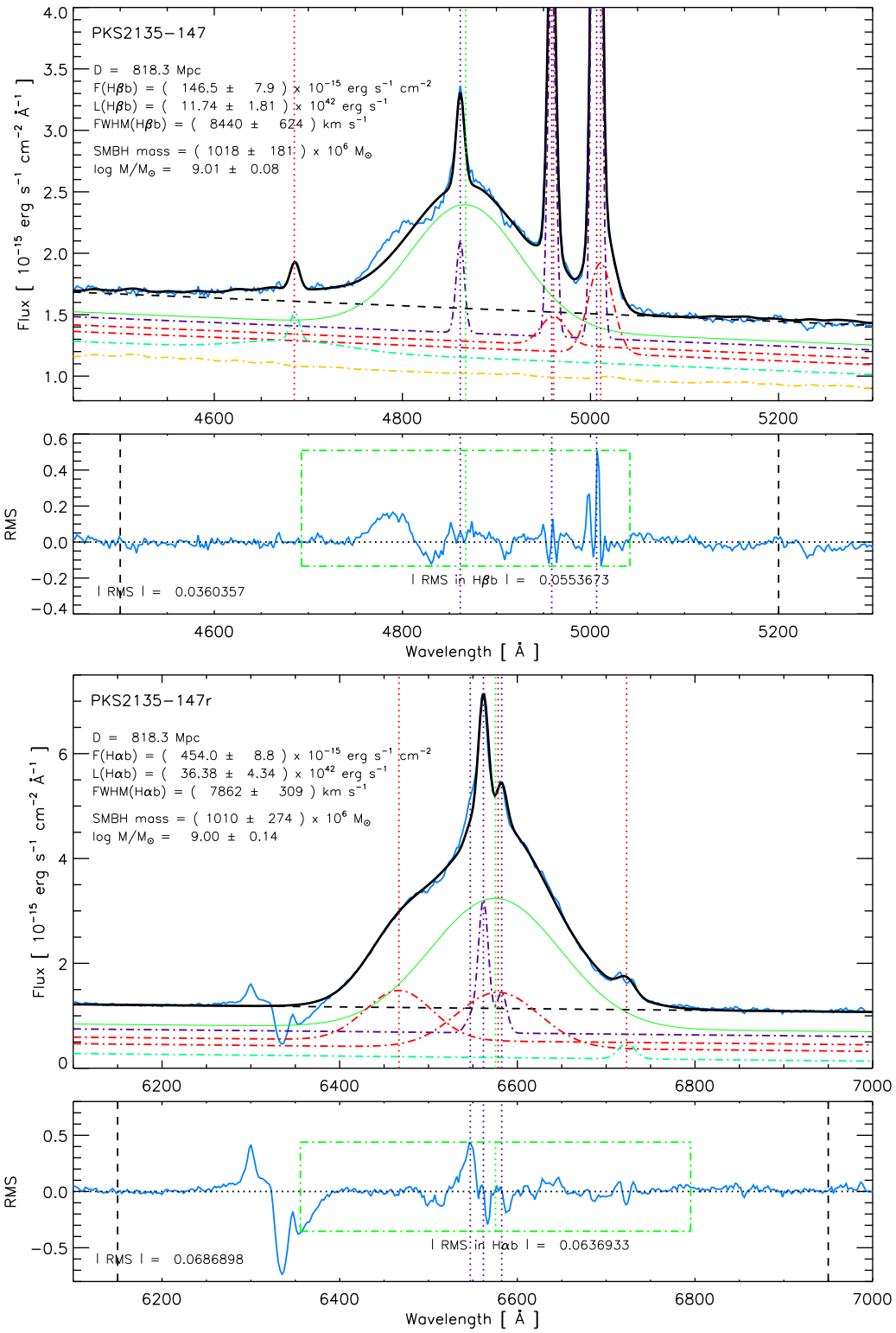
PKS2135−147
D = 818.3 Mpc
F(Hβb) = (146.5 ± 7.9) x 10^-15 erg s^-1 cm^-2
L(Hβb) = (11.74 ± 1.81) x 10^42 erg s^-1
FWHM(Hβb) = (8440 ± 624) km s^-1
SMBH mass = (1018 ± 181) x 10^6 M⊙
log M/M⊙ = 9.01 ± 0.08
Flux [10^-15 erg s^-1 cm^-2 Å^-1]
RMS
| RMS | = 0.0360357
| RMS in Hβb | = 0.0553673
Wavelength [Å]
PKS2135−147r
D = 818.3 Mpc
F(Hαb) = (454.0 ± 8.8) x 10^-15 erg s^-1 cm^-2
L(Hαb) = (36.38 ± 4.34) x 10^42 erg s^-1
FWHM(Hαb) = (7862 ± 309) km s^-1
SMBH mass = (1010 ± 274) x 10^6 M⊙
log M/M⊙ = 9.00 ± 0.14
Flux [10^-15 erg s^-1 cm^-2 Å^-1]
RMS
| RMS | = 0.0686898
| RMS in Hαb | = 0.0636933
Wavelength [Å]

Fig. 13.— Fit to the emission line profiles of PKS 2135-147 around the Hβ region (top) and the Hα region (bottom). The lines are the same described in Fig. 1, following the same procedure for Hα as described in Fig. 2. For the Hα fit the dotted-dashed green line is a broad [S II] λ6717+λ6731 line.

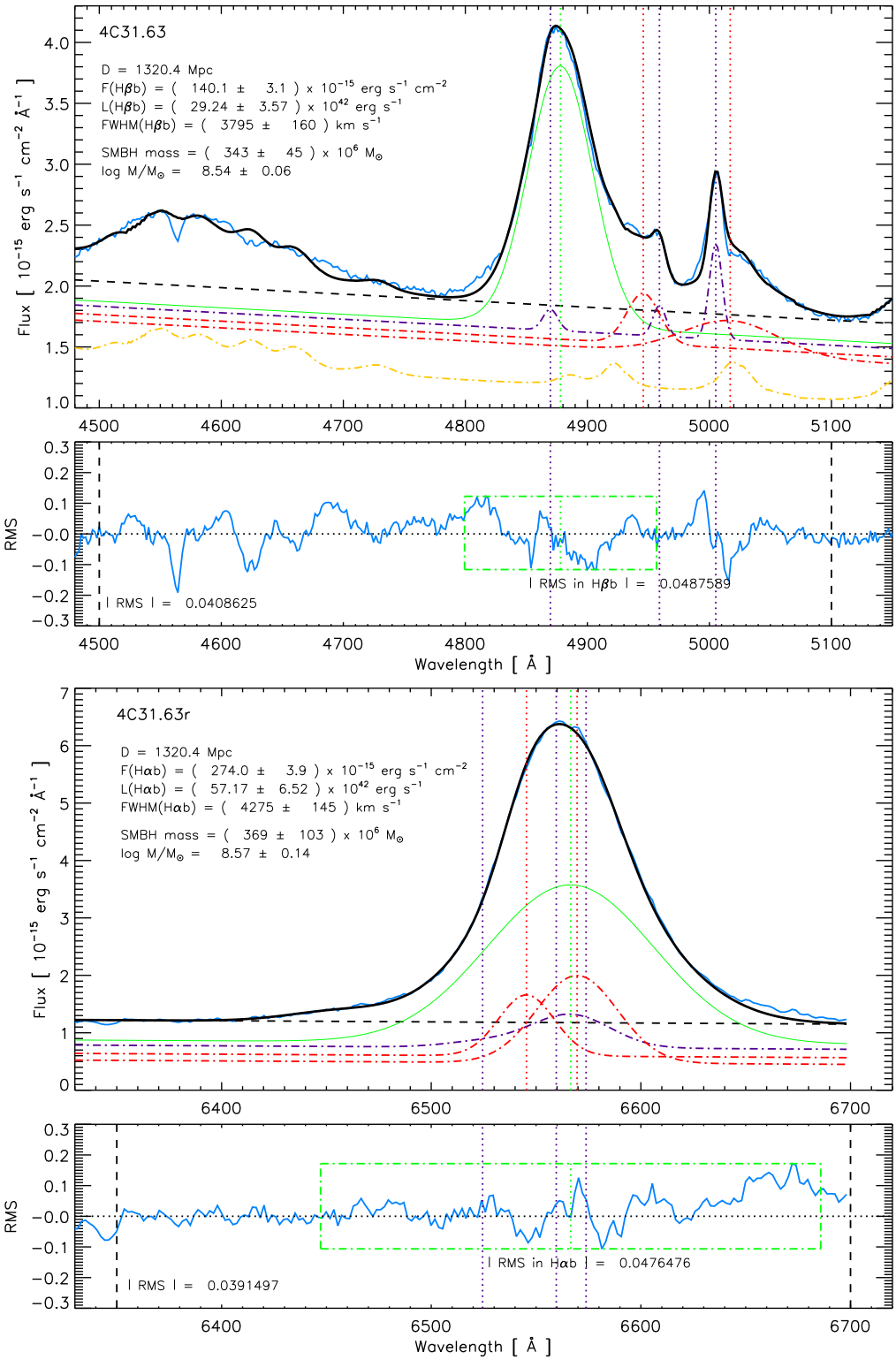
4C31.63
D = 1320.4 Mpc
F(Hβb) = (140.1 ± 3.1) x 10^-15 erg s^-1 cm^-2
L(Hβb) = (29.24 ± 3.57) x 10^42 erg s^-1
FWHM(Hβb) = (3795 ± 160) km s^-1
SMBH mass = (343 ± 45) x 10^6 M⊙
log M/M⊙ = 8.54 ± 0.06
Flux [10^-15 erg s^-1 cm^-2 Å^-1]
RMS
| RMS | = 0.0408625
| RMS in Hβb | = 0.0487589
Wavelength [Å]
4C31.63r
D = 1320.4 Mpc
F(Hαb) = (274.0 ± 3.9) x 10^-15 erg s^-1 cm^-2
L(Hαb) = (57.17 ± 6.52) x 10^42 erg s^-1
FWHM(Hαb) = (4275 ± 145) km s^-1
SMBH mass = (369 ± 103) x 10^6 M⊙
log M/M⊙ = 8.57 ± 0.14
Flux [10^-15 erg s^-1 cm^-2 Å^-1]
RMS
| RMS | = 0.0391497
| RMS in Hαb | = 0.0476476
Wavelength [Å]

Fig. 14.— Fit to the emission line profiles of 4C 31.63 around the Hβ region (top) and the Hα region (bottom). The lines are the same described in Fig. 1, following the same procedure for Hα as described in Fig. 2.

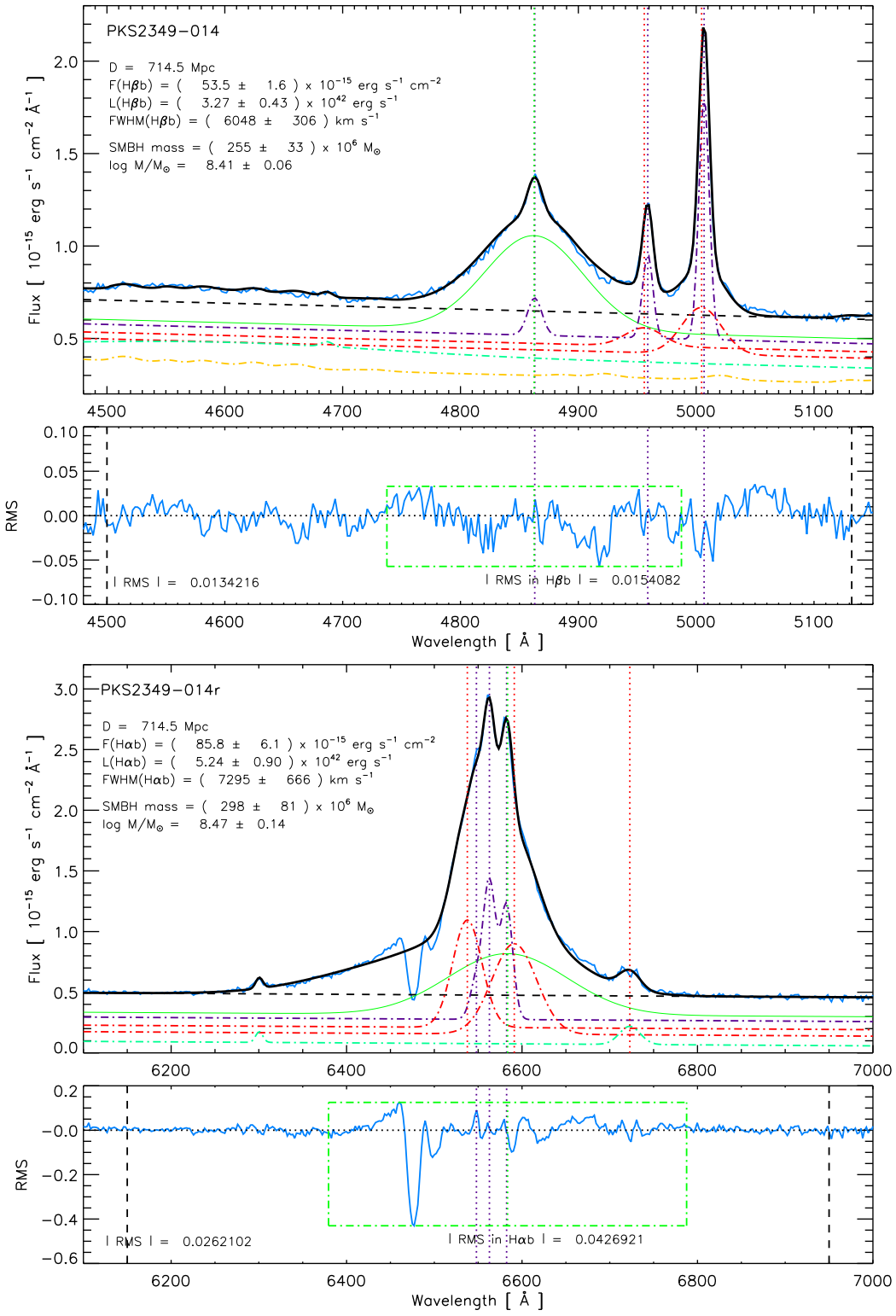
PKS2349−014
D = 714.5 Mpc
F(Hβb) = (53.5 ± 1.6) x 10^-15 erg s^-1 cm^-2
L(Hβb) = (3.27 ± 0.43) x 10^42 erg s^-1
FWHM(Hβb) = (6048 ± 306) km s^-1
SMBH mass = (255 ± 33) x 10^6 M⊙
log M/M⊙ = 8.41 ± 0.06
Flux [10^-15 erg s^-1 cm^-2 Å^-1]
RMS
| RMS | = 0.0134216
| RMS in Hβb | = 0.0154082
Wavelength [Å]
PKS2349−014r
D = 714.5 Mpc
F(Hαb) = (85.8 ± 6.1) x 10^-15 erg s^-1 cm^-2
L(Hαb) = (5.24 ± 0.90) x 10^42 erg s^-1
FWHM(Hαb) = (7295 ± 666) km s^-1
SMBH mass = (298 ± 81) x 10^6 M⊙
log M/M⊙ = 8.47 ± 0.14
Flux [10^-15 erg s^-1 cm^-2 Å^-1]
RMS
| RMS | = 0.0262102
| RMS in Hαb | = 0.0426921
Wavelength [Å]

Fig. 15.— Fit to the emission line profiles of PKS 2349-014 around the Hβ region (top) and the Hα region (bottom). The lines are the same described in Fig. 1, following the same procedure for Hα as described in Fig. 2. For the Hα fit the dotted-dashed green line is a narrow [O I] λ6730 and a broad [S II] λ6717+λ6731 line.

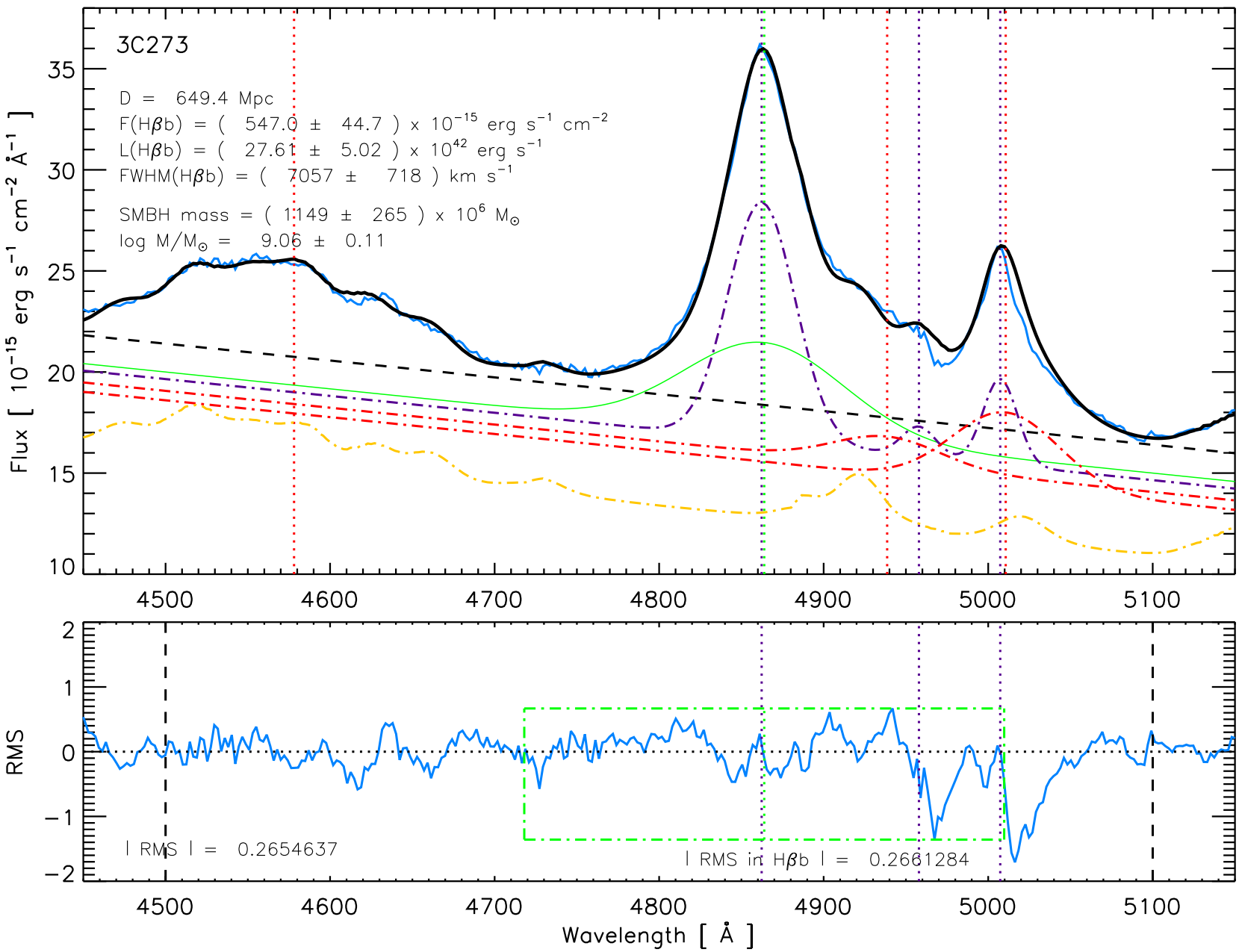
3C273
D = 649.4 Mpc
F(Hβb) = (547.0 ± 44.7) x 10^-15 erg s^-1 cm^-2
L(Hβb) = (27.61 ± 5.02) x 10^42 erg s^-1
FWHM(Hβb) = (7057 ± 718) km s^-1
SMBH mass = (1149 ± 265) x 10^6 M⊙
log M/M⊙ = 9.06 ± 0.11
Flux [10^-15 erg s^-1 cm^-2 Å^-1]
RMS
| RMS | = 0.2654637
| RMS in Hβb | = 0.2661284
Wavelength [Å]